

Wigner-function formalism for the detection of single microwave pulses in a resonator-coupled double quantum dot

Drilon Zenelaj,¹ Peter Samuelsson,¹ and Patrick P. Potts²

¹*Physics Department and NanoLund, Lund University, Box 118, 22100 Lund, Sweden*

²*Department of Physics and Swiss Nanoscience Institute,
University of Basel, Klingelbergstrasse 82, 4056 Basel, Switzerland*

(Dated: October 21, 2024)

Semiconductor double quantum dots (DQD) coupled to superconducting microwave resonators offer a promising platform for the detection of single microwave photons. In previous works, the photodetection was studied for a monochromatic source of microwave photons. Here, we theoretically analyze the photodetection of single microwave pulses. The photodetection in this case can be seen as a non-linear filtering process of an incoming signal, the pulse, to an outgoing one, the photocurrent. This analogy to signal processing motivated the derivation of a Wigner-function formalism which provides a compelling visualization of the time and frequency properties of the photodetector for low intensities. We find a trade-off between detecting the time and the frequency of the incoming photons in agreement with the time-energy uncertainty relation. As the intensity of the source increases, the photodetection is influenced by coherent Rabi oscillations of the DQD. Our findings give insight into the time-dependent properties of microwave photons interacting with electrons in a DQD-resonator hybrid system and provide guidance for experiments on single microwave pulse detection.

I. INTRODUCTION

The ability to efficiently and continuously detect single photons [1] is a key prerequisite in a variety of emergent quantum technologies, such as quantum cryptography and key distribution [2], quantum random number generation [3], and linear optics quantum computation [4]. Most developments in the field of single-photon detectors, like near-unit photodetection efficiency [5] and photon-number resolved detection [6], have so far been achieved in the optical domain. In said frequency regime, standard semiconductor diodes are employed, where the bandgap energy of the semiconductor is on the order of the energy of the optical photons [7].

This approach does, however, not work in the microwave domain, since microwave photons have an energy which is around five orders of magnitude smaller compared to optical photons. A different architecture is thus needed for the detection of single microwave photons. In recent years, different architectures have been investigated both theoretically and experimentally [8–21]. Detectors based on superconducting qubits [15–19, 22, 23] or SNS junctions [21] have demonstrated functionalities such as near-unit photodetection efficiency [15, 16, 19, 21] and quantum non-demolition measurements [17, 18] of itinerant photons.

One promising candidate, the one relevant for this work, comprises a semiconductor double quantum dot (DQD) coupled to a driven superconducting microwave resonator. Recently, efficient and continuous microwave photodetection in said system has been achieved, with

a photodetection reaching up to 25% [24], moving close to the theoretically predicted unit efficiency [25]. The detection mechanism is an analogue to the semiconductor photodiode, as photons in the resonator generate an electrical photocurrent by exciting an electron from the ground to the excited state of the DQD.

So far, photodetection in the DQD-resonator system has been studied in the case where the drive is a monochromatic source of microwave radiation [26, 27]. Extending on previous works on photodetection for a monochromatic drive, the focus of the present work is to investigate the time-dependent photodetector properties of the DQD-resonator system when subjected to an input of microwave pulses. Quite generally, the photodetection process constitutes a nonlinear filtering [28], converting an incoming signal, the coherent drive pulse with complex amplitude $f(t)$, into an outgoing signal, the (real) photocurrent $I(t)$. A compelling mathematical tool for the study of such a filtering process, in the weak drive limit, is the Wigner function [29]. This formalism gives access to study the time and frequency dependence of the detector and highlights the well-known time-frequency uncertainty relation, preventing the simultaneous measurement of a photon's arrival time and its frequency. We focus on two well-known and analytically tractable pulse shapes, Gaussian and Lorentzian. We characterize the performance of the photodetector by comparing the amplitude, shape and timing of the outgoing photocurrent pulse to the same properties of the incoming drive pulse. We find that the photodetector works best in the low-drive regime and when the bandwidth of the

detector is large compared to the linewidth of the drive pulse. Moving away from the low-drive regime, we find that the photocurrent can exhibit oscillations in time, which we attribute to Rabi oscillations of the DQD. The findings of this work may encourage additional experiments on hybrid semiconductor-resonator photodetectors. Furthermore, they will establish a foundation for future theoretical studies on photodetection using various microwave sources, including non-classical ones, and for exploring functionalities such as single-photon and photon-number-resolved detection.

This paper is organized as follows. In Sec. II, we present our theoretical model for describing the DQD-resonator system and demonstrate its working principle as an efficient photodetector. Additionally, we review the necessary conditions to achieve near unit photon-to-electron conversion efficiency. In Sec. III, we present the Wigner-function formalism for the drive and detector, respectively, and show how it can be used to compute the photocurrent. In Sec. IV, we analyze the performance of the photodetector by employing several performance quantifiers. In Sec. V, we analyze the photodetection away from the low-drive limit. We conclude and give a brief outlook in Sec. VI.

II. SYSTEM AND MODEL

The photodetector system, shown in Fig. 1 and studied in Refs. [25–27, 30–39], consists of a double quantum dot (DQD) coupled to a microwave resonator. The DQD is further coupled to fermionic source and drain leads. In contrast to earlier works, we here consider the system driven by applying pulses of microwave photons - a coherent tone with a time-modulated amplitude. The DQD acts as a detector for the microwave pulses by transforming them into electrical photocurrent pulses.

Following closely the notation in Ref. [27], the Hamiltonian describing the driven DQD-resonator system in the frame rotating at the center frequency of the pulse ω_1 is given by [40–42]

$$H = \Delta_d \frac{\sigma_z}{2} + \Delta_r a^\dagger a + g(a^\dagger \sigma_- + a \sigma_+) + \sqrt{\kappa_{\text{in}}} [f(t)a^\dagger + f^*(t)a], \quad (1)$$

where $\Delta_d = \Omega - \omega_1$ ($\Delta_r = \omega_r - \omega_1$) gives the detuning between the DQD (resonator) and the drive, κ_{in} denotes the coupling strength between the impinging photons and the resonator and $f(t)$ is the time-dependent amplitude of the pulse. Here, $\Omega = \sqrt{\epsilon^2 + 4t_c^2}$ is the splitting between the DQD ground and excited states, denoted $|g\rangle$ and $|e\rangle$, with ϵ being the energy detuning between quantum dot L and R and t_c is the inter-dot tunnel

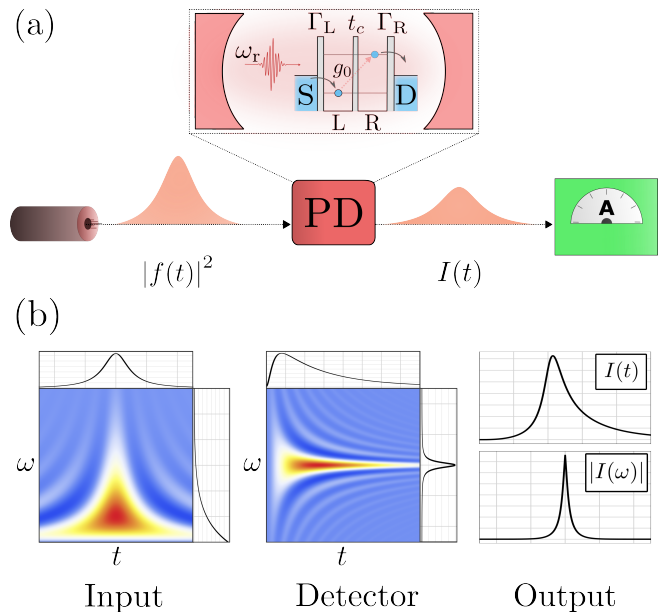


FIG. 1. (a) A photodetector (PD) transforms an incoming microwave pulse to an outgoing electrical pulse. The PD consists of a double quantum dot (DQD) embedded in a microwave resonator with resonance frequency ω_r . The DQD is tunnel coupled to a source (S) and drain (D) lead. An electron from S tunnels into the left dot L with the rate Γ_L . The electron can then absorb a photon through the coupling to the resonator with the bare coupling strength g_0 and move to the right dot R, where it can tunnel out to D with the rate Γ_R , producing an electrical photocurrent through the DQD. The incoming microwave pulse is described by a complex amplitude $f(t)$, the outgoing photocurrent by $I(t)$ (see main text). (b) Left and middle: Wigner function representation of the incoming drive for a Lorentzian pulse and the PD, respectively, and their marginals. Right: Outgoing photocurrent as a function of time (top panel) and frequency (bottom panel).

coupling. The DQD operators include the Pauli z -matrix $\sigma_z = |e\rangle\langle e| - |g\rangle\langle g|$ as well as the raising and lowering operators $\sigma_+ = |e\rangle\langle g|$ and $\sigma_- = \sigma_+^\dagger = |g\rangle\langle e|$. We note that the state space of the DQD also includes $|0\rangle$, denoting the state with no electrons on the DQD, taken to have zero energy. The operators a^\dagger (a) create (annihilate) photons in a resonator mode with frequency ω_r . The DQD-resonator interaction is described by a standard Jaynes-Cummings Hamiltonian [43] within the rotating-wave approximation, with the interaction strength $g = g_0 \sin(\theta)$, where g_0 is the bare coupling strength and the mixing angle θ is defined by $\cos(\theta) = -\epsilon/\Omega$.

The rates for electron tunneling between the leads and the L and R dot are Γ_L and Γ_R , respectively. Further, the source and drain leads are kept at the same potential and energies are counted with respect to the lead chemical potential. As illustrated in Fig. 1, the DQD ground

and excited states energies are symmetric around zero. Assuming a small temperature T of the leads, such that $k_B T \ll \Omega$, electrons from the leads can only enter the DQD into the ground state and leave from the excited state, with respective rates

$$\Gamma_{g0} = \Gamma_{L,\text{in}} + \Gamma_{R,\text{in}}, \quad \Gamma_{0e} = \Gamma_{L,\text{out}} + \Gamma_{R,\text{out}}, \quad (2)$$

where

$$\begin{aligned} \Gamma_{L,\text{in}} &= \Gamma_L \cos^2(\theta/2), & \Gamma_{R,\text{in}} &= \Gamma_R \sin^2(\theta/2), \\ \Gamma_{L,\text{out}} &= \Gamma_L \sin^2(\theta/2), & \Gamma_{R,\text{out}} &= \Gamma_R \cos^2(\theta/2). \end{aligned} \quad (3)$$

In addition to electron tunneling, we account for pure dephasing of the DQD state with rate γ_ϕ , relaxation of an electron from the excited to the ground state of the DQD with rate γ_- and photonic losses with rate κ . The dynamics of the driven DQD-resonator system can then be described by a Lindblad master equation of the form [44, 45]

$$\begin{aligned} \partial_t \rho(t) &= -i[H, \rho(t)] + \Gamma_{g0} \mathcal{D}[s_g^\dagger] \rho(t) + \Gamma_{0e} \mathcal{D}[s_e] \rho(t) \\ &+ \frac{\gamma_\phi}{2} \mathcal{D}[\sigma_z] \rho(t) + \gamma_- \mathcal{D}[\sigma_-] \rho(t) + \kappa \mathcal{D}[a] \rho(t), \end{aligned} \quad (4)$$

with the superoperator $\mathcal{D}[x]\rho(t) = x\rho(t)x^\dagger - \frac{1}{2}\{x^\dagger x, \rho(t)\}$, where $s_g^\dagger = |g\rangle\langle 0|$ and $s_e = |0\rangle\langle e|$. The electrical photocurrent $I(t)$ flowing through the DQD, the photocurrent, is given by

$$I(t)/e = \Gamma_{R,\text{out}} \langle e|\rho(t)|e\rangle - \Gamma_{R,\text{in}} \langle 0|\rho(t)|0\rangle, \quad (5)$$

evaluated at the lead coupled to the R dot.

The photon-to-electron conversion efficiency, the probability that an incident photon is converted into an electron tunneling through the DQD, is a key figure of merit for the photodetector, as discussed further below. Connecting to previous works [25–27], for a monochromatic drive at frequency ω_1 with constant amplitude $\sqrt{\dot{N}}$, the efficiency is defined as

$$\eta_{\text{mc}}(\omega_1) = \frac{I_{\text{mc}}(\omega_1)/e}{\dot{N}}, \quad (6)$$

where I_{mc} is the dc electrical photocurrent and \dot{N} denotes the rate of impinging photons. In Refs. [25, 27] it was shown that ideal, unit-efficiency photodetection could be achieved for a monochromatic drive with the photodetector setup in Fig. 1. For completeness and further use below, we summarize the parameter conditions required for ideal photodetection in Tab. I. In the table, $\tilde{\Gamma} = \Gamma_{0e} + \gamma_- + 2\gamma_\phi$ denotes the total electron decoherence rate and $C = 4g^2/(\tilde{\Gamma}\kappa)$ the cooperativity. As can be seen from the table, a cooperativity equal to one is ideal for photodetection. We want to emphasize that this implies that an ideal photodetector does not require strong coupling between the DQD and the cavity.

Negligible internal photon losses	$\kappa \approx \kappa_{\text{in}}$
Resonator-DQD resonance	$\Omega = \omega_r = \omega_l$
Negligible electron decoherence	$\Gamma_{L,R} \gg \gamma_\phi, \gamma_-$
Small interdot tunneling	$\Omega \gg t_c$
Unit cooperativity	$C = 4g^2/(\tilde{\Gamma}\kappa) = 1$
Linear drive response	$I/e \propto \dot{N}$

TABLE I. Conditions for ideal photodetection when the DQD-resonator system is subjected to a monochromatic drive.

III. WIGNER-FUNCTION FORMALISM

Throughout the main part of the paper, we focus on the regime where the applied microwave drive is weak. In this low-drive regime, we can solve Eq. (5) and obtain an expression (see Appendix A) for the photocurrent in the form

$$I(t)/e = \frac{1}{2\pi} \int_0^\infty d\tau d\tau' h(\tau, \tau') f(t-\tau) f^*(t-\tau'), \quad (7)$$

where $h(\tau, \tau') = h(\tau', \tau)$ is a real function of the detector properties only. The detector thus acts as a quadratic, time- and frequency-dependent filter [28] for the pulse with complex amplitude $f(t)$. We note that the photocurrent in Eq. (7) can also be understood as the low-drive amplitude term of a double, or bi-variate, Volterra series [46, 47], with $h(\tau, \tau')$ being the corresponding Volterra kernel.

For our purposes, it is convenient to rewrite the photocurrent in the compact and compelling form

$$I(t)/e = \int d\tau d\omega W_d(\tau, \omega) W_f(t-\tau, \omega), \quad (8)$$

which is a joint time convolution and frequency integration of the Wigner functions of the incident pulse $W_f(t, \omega)$ and of the detector $W_d(t, \omega)$. We note that a similar formulation in terms of Wigner functions is common in signal processing [28], when evaluating spectrograms of different types of non-stationary signals subjected to e.g. filtering or smoothing. Moreover, the formulation in Eq. (8) is closely related to the one in Ref. [48], where the statistics of measurement outcomes is obtained by integrating a product of the detector Wigner function and a quasi-probability representation of the system state.

A. Pulse Wigner function

The time-frequency Wigner, or Wigner-Ville, distribution for pulses with complex amplitudes is well known

from e.g. signal processing [49–53] and formally identical to the original, quantum-mechanical quasi-probability distribution [54] expressed in terms of the wavefunction. The pulse Wigner function is defined, in terms of the amplitude $f(t)$, as

$$W_f(t, \omega) = \frac{1}{2\pi} \int dy e^{-iy\omega} f(t + y/2) f^*(t - y/2). \quad (9)$$

We note that, borrowing notation from input-output formalism [55], we may write $f(t + y/2) f^*(t - y/2) = \langle b_{\text{in}}^\dagger(t - y/2) b_{\text{in}}(t + y/2) \rangle$, where $b_{\text{in}}(t)$ is an annihilation operator that describes the microwave drive. Equation (9) is then equivalent to the Wigner function introduced in Ref. [56] to describe single-electron coherence.

The marginals of the Wigner function in time and frequency are

$$\begin{aligned} \tilde{W}_f(t) &= \int d\omega W_f(t, \omega) = |f(t)|^2, \\ \tilde{W}_f(\omega) &= \int dt W_f(t, \omega) = |\tilde{f}(\omega)|^2. \end{aligned} \quad (10)$$

where $\tilde{f}(\omega) = 1/\sqrt{2\pi} \int dt e^{i\omega t} f(t)$ gives the Fourier transform of $f(t)$. The Wigner function is normalized as

$$\begin{aligned} \int dt d\omega W_f(t, \omega) &= \int dt \tilde{W}_f(t) = \int d\omega \tilde{W}_f(\omega) \\ &= \int dt |f(t)|^2 = \int d\omega |\tilde{f}(\omega)|^2 = \bar{N} \end{aligned} \quad (11)$$

where \bar{N} is the average number of photons in the pulse.

Throughout the paper, we will mainly focus on two common and analytically tractable types of drive pulses, Gaussian and Lorentzian pulses. For a Gaussian pulse, the time-dependent amplitude is

$$f(t) = \sqrt{\frac{\bar{N}}{\sigma\pi^{1/2}}} e^{-\frac{t^2}{2\sigma^2}}, \quad (12)$$

where σ denotes the width of the pulse. The Fourier transform of the pulse is given by

$$\tilde{f}(\omega) = \sqrt{\frac{\bar{N}\sigma}{\pi^{1/2}}} e^{-\frac{\omega^2\sigma^2}{2}}. \quad (13)$$

The Wigner function for the Gaussian pulse is

$$W_f(t, \omega) = \frac{\bar{N}}{\pi} e^{-t^2/\sigma^2 - \omega^2\sigma^2}. \quad (14)$$

For a Lorentzian, the pulse amplitude is given by

$$f(t) = \frac{\sqrt{\bar{N}\sigma}}{\sqrt{\pi}(t - i\sigma)}. \quad (15)$$

Its Fourier transform is

$$\tilde{f}(\omega) = \sqrt{2\bar{N}\sigma} i e^{-\sigma\omega} \Theta(\omega), \quad (16)$$

where $\Theta(\omega)$ is the Heavyside step function. The corresponding Wigner function is

$$W_f(t, \omega) = \frac{2\bar{N}\sigma e^{-2\sigma\omega} \sin(2t\omega) \Theta(\omega)}{\pi t}. \quad (17)$$

In Fig. 2, plots of the normalized Wigner functions $W_f(t, \omega)/\bar{N}$ for a Gaussian and Lorentzian pulse are presented, together with their respective time and frequency marginals.

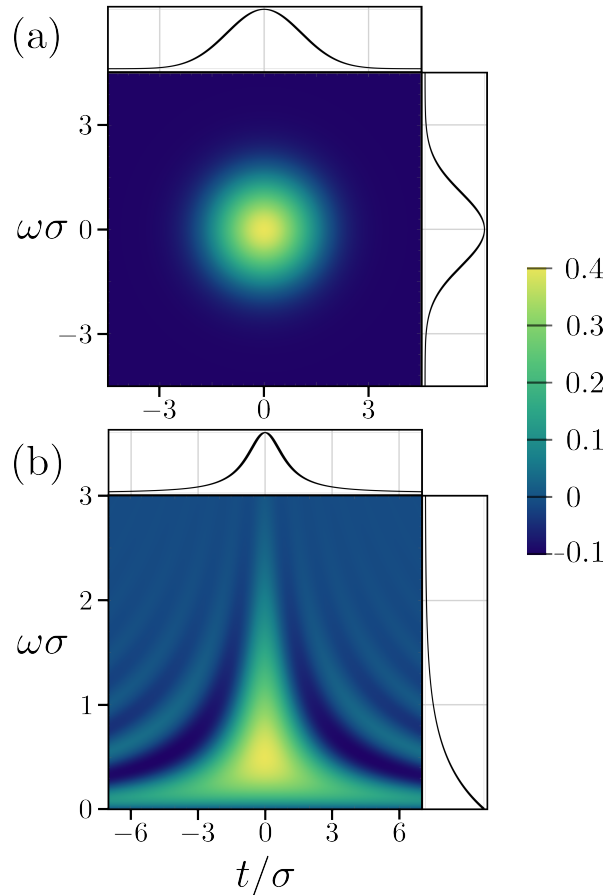


FIG. 2. Normalized Wigner functions and their respective time and frequency marginals for (a), a Gaussian pulse and (b), a Lorentzian pulse.

We point out that our Wigner-function formulation can also be applied to a monochromatic drive as well as a pulse localized in time. For a monochromatic drive at frequency ω_1 , we have, in the lab frame,

$$f(t) = \sqrt{\bar{N}} e^{i\omega_1 t}, \quad (18)$$

where $f(t)$ is flux normalized, i.e., describing a constant rate \dot{N} of incident photons. Plugging Eq. (18) into Eq. (9) gives

$$W_f(t, \omega) = \dot{N} \delta(\omega - \omega_1). \quad (19)$$

Here the flux normalization leads to that the average value $\bar{W}_f \rightarrow \infty$.

For a delta-function pulse, localized in time and arriving at the detector at time t_0 , we have

$$f(t) = \sqrt{2\pi N_\nu} \delta(t - t_0), \quad (20)$$

where N_ν denotes the photon number per unit bandwidth. In this case, the Wigner function is given by

$$W_f(t, \omega) = N_\nu \delta(t - t_0). \quad (21)$$

Again, the average value $\bar{W}_f \rightarrow \infty$. We note that Eqs. (19) and (21) are equivalent to the Wigner functions of momentum and position eigenstates, respectively.

B. Detector Wigner function

The detector Wigner function is defined in terms of the kernel $h(\tau_1, \tau_2)$ in Eq. (7) as

$$W_d(t, \omega) = \frac{1}{2\pi} \int dy e^{-iy\omega} h(t + y/2, t - y/2). \quad (22)$$

We point out that, in general, $h(\tau_1, \tau_2) \neq h_1(\tau_1)h_1^*(\tau_2)$, that is, the kernel cannot be written in the form of the pulse Wigner function given in Eq. (9). This makes the detector Wigner function formally similar to a Wigner function of a mixed quantum state while the pulse Wigner function is equivalent to the Wigner function of a pure state. Moreover, the symmetry property $h(\tau_1, \tau_2) = h(\tau_2, \tau_1)$ guarantees that $W_d(t, \omega)$ is real and causality of the detector requires that $W_d(t, \omega) = 0$ for $t < 0$.

The frequency and time marginals of $W_d(t, \omega)$, defined analogously to Eq. (10), are directly related to the photocurrents obtained in the limits of a monochromatic drive and a delta-function pulse, respectively. Explicitly, inserting the Wigner function for a monochromatic drive at ω_1 , Eq. (19), into the photocurrent expression in Eq. (8), the frequency marginal can be written as

$$W_d(\omega_1) = \frac{I_{mc}(\omega_1)/e}{\dot{N}} = \eta_{mc}(\omega_1), \quad (23)$$

This shows that the marginal $\tilde{W}_d(\omega_1)$ is equal to the detector efficiency $0 \leq \eta_{mc} \leq 1$.

For the time marginal, inserting the Wigner function for a delta-function pulse arriving at the detector at t_0 , Eq. (21), into Eq. (8), the time marginal can be written as

$$W_d(t) = \frac{I_\delta(t + t_0)/e}{N_\nu}, \quad (24)$$

where $I_\delta(t + t_0)$ is the photocurrent delta-function, or impulse, response. In addition, from Eq. (23) we have

that the detector Wigner function is normalized as

$$\bar{W}_d = \int dt d\omega W_d(t, \omega) = \frac{1}{N_\nu} \int dt I_\delta(t + t_0)/e, \quad (25)$$

which is the number of electrons transferred through the DQD in response to a delta-function pulse, divided by the number of photons per unit bandwidth in the pulse. We note that the normalization constant \bar{W}_d has the unit of frequency.

1. Time-frequency uncertainty relation

As dictated by fundamental principles of quantum mechanics, it is impossible to simultaneously determine the frequency of an incident photon and the photon-arrival time at the detector.

According to Eq. (7), on the level of averages, photo-detection can be understood as a classical signal processing problem, where a complex signal $f(t)$ is being measured by the photocurrent $I(t)$. It is, however, still impossible to simultaneously determine the frequency as well as the arrival time of an incoming pulse due to the Heisenberg-Gabor limit [57], which states that one cannot sharply localize a signal in both the time domain and the frequency domain. To detect the arrival time of a pulse perfectly, the detector Wigner function needs to obey $W_d(t, \omega) \propto \delta(t)$. In this case, the response to a delta-function pulse [c.f. Eq. (24)] is again a delta-function pulse. Alternatively, the detector becomes frequency selective if $W_d(t, \omega) \propto \delta(\omega - \omega_1)$. In this case, only signals with frequency ω_1 are detected. To be both frequency selective and to detect arrival times perfectly, the Wigner function would thus need to obey $W_d \propto \delta(t)\delta(\omega - \omega_1)$. This is prevented by the Heisenberg-Gabor limit which reads, in full analogy to the Heisenberg uncertainty relation,

$$\Delta t \Delta \omega \geq \frac{1}{2}, \quad (26)$$

where $\Delta \omega = \sqrt{\langle \omega^2 \rangle - \langle \omega \rangle^2}$, $\Delta t = \sqrt{\langle t^2 \rangle - \langle t \rangle^2}$ and $\langle x \rangle = \int dt d\omega x W_d(t, \omega) / \bar{W}_d$. A detailed derivation of Eq. (26) is given in Appendix C. We note that Eq. (26) only holds for detectors that do not allow for a negative photocurrent. Should the photocurrent become negative, which is in principle possible in our system due to back-tunneling from the drain, Δt is no longer a good measure of the spread of the photocurrent.

In the following, we consider a good detector to have a fast time-resolution, i.e., a small Δt , as this allows one to determine the shape of an incoming microwave pulse. In this case, the ideal detector Wigner function reads

$$W_d = \delta(t) \quad \Rightarrow \quad I(t)/e = |f(t)|^2. \quad (27)$$

We note from Eq. (23) that such an ideal detector has unit efficiency at all frequencies, $\eta_{\text{mc}}(\omega) = 1$ and thus, an infinitely wide bandwidth, as well as a diverging normalization \bar{W}_d . For real detectors, $\eta_{\text{mc}}(\omega) \rightarrow 0$ for $|\omega| \rightarrow \infty$ and the Wigner function cannot develop diverging peaks as it obeys the inequality (see Appendix C for a derivation)

$$|W_d(t, \omega)| \leq \frac{\bar{W}_d}{\pi}. \quad (28)$$

As for Eq. (26), this relation only holds for detectors that

do not allow for a negative photocurrent.

C. Our detector

Turning to the photodetector described in the previous section, we focus our discussion on the parameter regime described in Tab. I, leading to ideal photodetection for a monochromatic drive, with the slight difference that we relax the requirement for unit cooperativity, i.e. $C \neq 1$. In this parameter regime, we to obtain an analytical, closed form expression for the detector Wigner function (for $t \geq 0$, as we find $W_d(t, \omega) = 0$ for $t < 0$ due to causality)

$$W_d(t, \omega) = 32\pi g^2 \Gamma_R \kappa e^{-t(\Gamma_R + \kappa)/2} \begin{cases} \frac{\alpha \cos(\alpha t/2) \sin(2t\omega) - 4\omega \sin(\alpha t/2) \cos(2t\omega)}{\alpha\omega(16\omega^2 - \alpha^2)}, & 4g > |\Gamma_R - \kappa| \\ \frac{\alpha' \cosh(\alpha' t/2) \sin(2t\omega) - 4\omega \sinh(\alpha' t/2) \cos(2t\omega)}{\alpha'\omega(16\omega^2 + \alpha'^2)}, & 4g < |\Gamma_R - \kappa| \end{cases} \quad (29)$$

where $\alpha = \sqrt{-(\Gamma_R - \kappa)^2 + 16g^2}$, $\alpha' = \sqrt{(\Gamma_R - \kappa)^2 - 16g^2}$. We observe that the Wigner function is symmetric in frequency, $W_d(t, \omega) = W_d(t, -\omega)$ and is invariant under an exchange $\Gamma_R \leftrightarrow \kappa$.

Integrating Eq. (29) over time (frequency) we have the frequency (time) marginal of the Wigner function as

$$\tilde{W}_d(t) = 64\pi^2 g^2 \Gamma_R \kappa e^{-t(\Gamma_R + \kappa)/2} \begin{cases} \frac{\sin^2(\alpha t/4)}{\alpha^2}, & 4g > |\Gamma_R - \kappa| \\ \frac{\sinh^2(\alpha' t/4)}{\alpha'^2}, & 4g < |\Gamma_R - \kappa| \end{cases} \quad (30)$$

and

$$W_d(\omega) = 512\pi g^2 \Gamma_R \kappa \begin{cases} \frac{1}{[(\Gamma_R + \kappa)^2 + (\alpha - 4\omega)^2][(\Gamma_R + \kappa)^2 + (\alpha + 4\omega)^2]}, & 4g > |\Gamma_R - \kappa| \\ \frac{1}{[(\alpha' + \Gamma_R + \kappa)^2 + 16\omega^2][(-\alpha' + \Gamma_R + \kappa)^2 + 16\omega^2]}, & 4g < |\Gamma_R - \kappa| \end{cases} \quad (31)$$

Via Eqs. (23) and (24), Eqs. (31) and (30) thus give the explicit expressions for the photocurrent of a monochromatic drive and the photodetector impulse response, respectively.

The normalization of the Wigner function is given by

$$\bar{W}_d = \frac{16\pi^2 g^2 \Gamma_R \kappa}{(\Gamma_R + \kappa)(\Gamma_R \kappa + 4g^2)}. \quad (32)$$

In Fig. 3, we plot the normalized Wigner functions in Eq. (29) together with their respective, normalized time and frequency marginals for different values of Γ_R/κ and C .

We see that W_d , for all parameter values, has a T-shape in time-frequency space with a global maximum at $\omega = 0$ and $t > 1/(\Gamma_R + \kappa)$, located at $t = 6/(\Gamma_R + \kappa)$

at $\alpha \rightarrow 0$. The Wigner function also displays distinct oscillations around zero in time and frequency due to the harmonic terms $\sin(2\omega t)$ and $\cos(2\omega t)$. The oscillations decay towards large frequencies and times. While W_d has a complex structure in both time and frequency space, we note that the exponential decay with increasing time is governed by the time scale $1/(\Gamma + \kappa)$. As a result, the minimum effective bandwidth of the detector is of order $\Gamma_R + \kappa$, which is also clear from the expression for the frequency marginal in Eq. (31). We also observe a splitting of the resonance peak in the frequency marginal, which is on the order of $\alpha/2$ and is most clearly visible when $C > 1$. This appears to be a consequence of the Rabi splitting, which is present in the regime of strong electron-photon coupling [58].

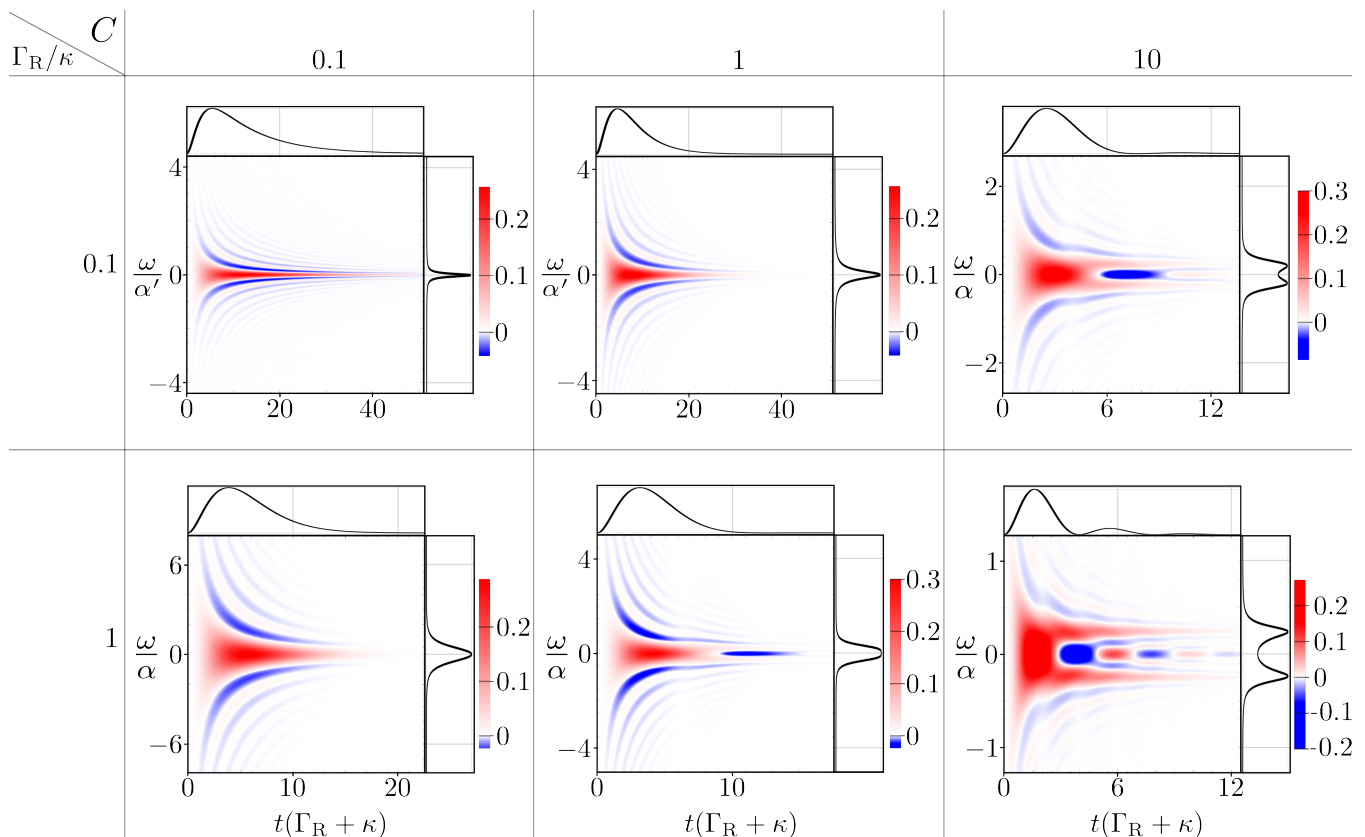


FIG. 3. Normalized Wigner function of the detector with its respective time and frequency marginals for $\Gamma_R/\kappa = 0.1, 1$ and cooperativity $C = 0.1, 1$, and 10 .

IV. PHOTOCURRENT RESPONSE AND DETECTOR OPERATION

To both qualitatively and quantitatively characterize the operation of our system as a detector for incoming photon pulses, we compare the outgoing electrical photocurrent $I(t)$ to the incoming pulse magnitude $|f(t)|^2$. We work in the ideal-detector limit, implying that we use $C = 1$ throughout this section. In addition to the monochromatic drive, where the detector efficiency is the key performance measure, for a time-dependent photon pulse also the ability of the detector to respond rapidly and to faithfully transfer the temporal shape of the drive into the output photocurrent are important features. In order to quantify the performance of the photodetector, we will thus employ three different performance measures:

1. The photodetection efficiency, which in the case of a pulse input is given by

$$\eta_p = \frac{Q/e}{\bar{N}}, \quad (33)$$

where $Q = \int dt I(t)$ is the average transferred charge in the electrical photocurrent pulse. The

efficiency $0 \leq \eta_p \leq 1$ thus provides information on the ability of the photodetector to detect the average number of photons in the drive pulse, key for number resolved photodetection. Unit efficiency implies that every photon in the pulse is converted into exactly one electron in the photocurrent.

2. The average delay in time between the input and output signal, which is defined as

$$\tau_d = \int dt t \left[\frac{I(t)/e}{Q} - \frac{|f(t)|^2}{\bar{N}} \right]. \quad (34)$$

We note that the input and output signals have been normalized to correctly produce the average times.

3. The fidelity of the temporal shape transfer, given by

$$O = \int dt \sqrt{\frac{|f(t - \tau_d)|^2}{\bar{N}} \cdot \frac{I(t)/e}{Q}}. \quad (35)$$

Here, the input and output signals have been normalized and shifted with the average time delay, in

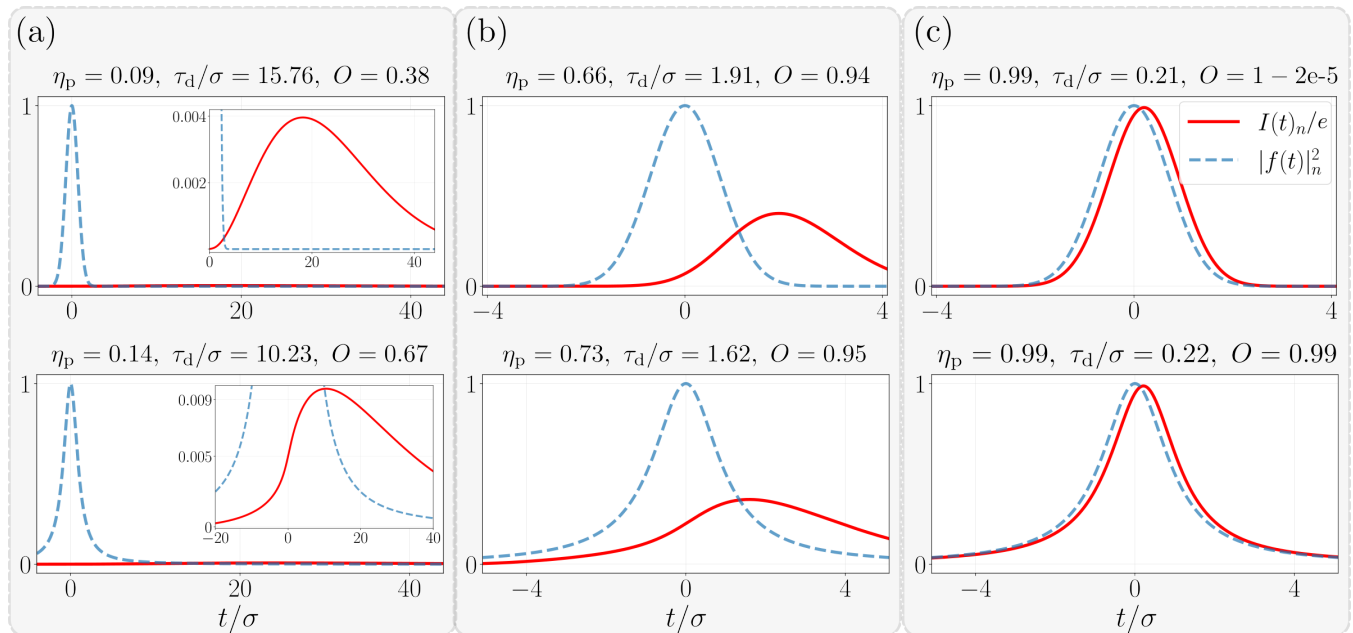


FIG. 4. Normalized photocurrent in the ideal-detector limit and drive pulses for a Gaussian (top) and Lorentzian (bottom) drive for $\bar{N} = 0.1$, $\Gamma_R/\kappa = 1$ and (a) $\sigma(\Gamma_R + \kappa)/2 = 0.1$, (b) $\sigma(\Gamma_R + \kappa)/2 = 1$, (c) $\sigma(\Gamma_R + \kappa)/2 = 10$. Insets in (a) show a zoomed-in version to visualize the electrical photocurrent pulse.

order to compare the shapes only. Moreover, we employ the Bhattacharyya distance [59], quantifying the similarity, or overlap, of two distributions. This gives $0 \leq O \leq 1$, with $O = 1$ for identical input and output shapes.

We note that for the idealized detector described by the Wigner function in Eq. (27), we find $\eta_p = 1$, $\tau_d = 0$, and $O = 1$, implying optimal performance according to our figures of merit.

We expect the relation between the spectral width of the drive pulse and the typical bandwidth of the detector, $\sim \Gamma_R + \kappa$, to be the defining aspect of the detector performance. We will therefore focus on three different regimes, where the frequency width of the incoming pulse is larger, comparable to, and smaller than the detector bandwidth, respectively. In Fig. 4, we plot the photocurrent in the ideal-detector limit together with the incoming pulse in the three different regimes for a Gaussian and a Lorentzian drive, respectively. The photocurrent and drive pulses have been normalized with the same prefactor, such that $|f(t=0)|_n^2 = 1$, where the subscript stands for *normalized*. We also give the numerical values for the different performance quantifiers.

We observe a similar trend for both Gaussian and Lorentzian drive pulses. The detector's performance significantly improves from panels (a) to (c) across all quantifiers. This improvement is anticipated, as the detector Wigner function approaches the ideal limit described in

Eq. (27) with increasing detector bandwidth. We also observe that the conditions for ideal photodetection for a monochromatic pulse given in Tab. I result in very good detection of microwave pulses according to all three figures of merit used.

A. Experimental setting

In an experimental setting, the parameters governing the DQD-resonator system are typically not ideal. We would thus like to study the photodetection of single pulses in a more realistic parameter regime. To that end, we use the parameters obtained from the experiment in Ref. [24], where experimentally, a photo-detection efficiency of 25% was achieved using a monochromatic drive. The numerical values for the system parameters are summarized in Tab. II.

We again look at the Wigner function of the detector by numerically solving Eq. (22), see Fig. 5. The Wigner function looks similar to the one in the upper left panel of Fig. 3. This is to be expected, as we are in a similar parameter regime.

In Fig. 6, we plot the photocurrent together with the incoming pulse for a Gaussian and a Lorentzian drive, respectively and give the numerical values for the different performance quantifiers.

$\kappa_{\text{in}}/2\pi$	3.8 MHz
$\kappa/2\pi$	5.2 MHz
$\Gamma_{\text{L}}/2\pi$	12 MHz
$\Gamma_{\text{R}}/2\pi$	1.1 GHz
$g/2\pi$	43 MHz
$\gamma_{-}/2\pi$	23 MHz
$\gamma_{\phi}/2\pi$	1.8 GHz
$\Omega/2\pi$	6.67 GHz
$\epsilon/2\pi$	-6.6 GHz
C	0.15

TABLE II. Experimental rates governing the DQD-resonator system, taken from Ref. [24].

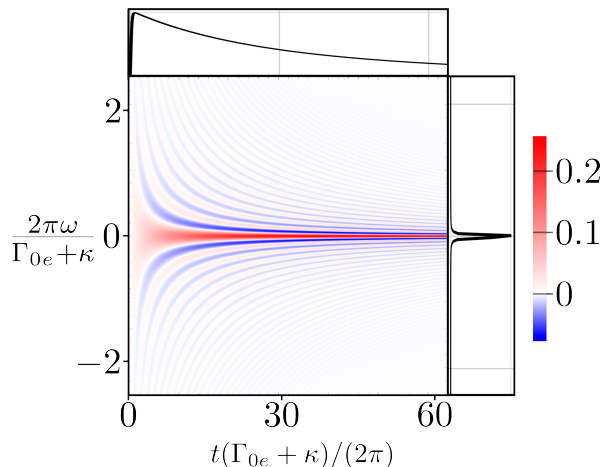


FIG. 5. Normalized Wigner function of the detector and its respective time and frequency marginals using the experimental parameters in Tab. II.

V. BEYOND THE LOW-DRIVE LIMIT

For larger microwave drive amplitudes, the low-drive expression for the photocurrent in Eq. (7) as well as the Wigner function formulation in Eq. (8) do not hold anymore. To investigate the time-dependent photocurrent response we instead solve the Lindblad master equation in Eq. (4) numerically using QuTip [60] and evaluate the photocurrent via Eq. (5).

To obtain a qualitative picture of the photocurrent response beyond the low-drive regime, we plot in Fig. 7 the photocurrent as a function of time for drive strengths and a set of detector parameters $\Gamma_{\text{L}}, \Gamma_{\text{R}}, \kappa$. For simplicity, we consider an incoming Gaussian pulse of temporal width σ , however, qualitatively similar results are obtained for a Lorentzian pulse as also discussed further below. The overall pattern is that the photocurrent pulses increase in amplitude and change shape when increasing the drive amplitude. There are two distinct features, different from the low-drive limit, to be emphasized:

First, the photocurrent becomes dependent on the

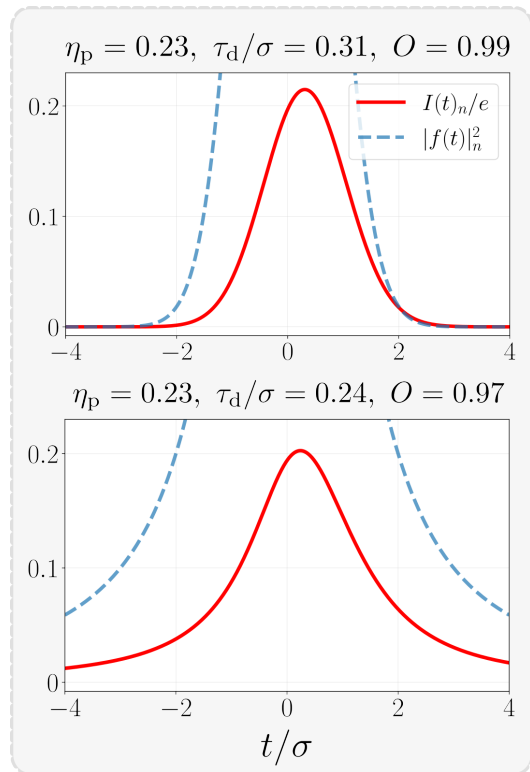


FIG. 6. Normalized photocurrent pulses for a Gaussian (top) and Lorentzian (bottom) drive for $\bar{N} = 0.1$ and $\sigma(\Gamma_{0e} + \kappa)/(4\pi) = 77$ using the experimental parameters in Tab. II.

rate, Γ_{L} , for electrons to tunnel into the DQD. This is most clearly visible for $\sigma(\Gamma_{\text{R}} + \kappa) \gtrsim 1$ in Fig. 7 and can be understood as follows: In the low-drive limit, the photon assisted electron tunneling between the left and the right dot is the slowest transport process, acting as a bottleneck for the photocurrent. Hence, the dot filling rate Γ_{L} does not play any role for the photocurrent, as also evident from Eq. (29). Increasing the drive strength, the photon assisted tunnel rate becomes comparable to the other rates in the problem and Γ_{L} starts to affect the photocurrent $I(t)$.

Second, for certain parameters, most prominent for $\sigma(\Gamma_{\text{R}} + \kappa) \approx 1$ in Fig. 7, the photocurrent develops temporal oscillations for increasing drive amplitudes. The amplitude and frequency of the oscillations depend on both drive strength \bar{N} as well as the ratio $\Gamma_{\text{L}}/\Gamma_{\text{R}}$. Importantly, the oscillations persist for large-drive amplitudes $\bar{N} \gg 1$.

A. Large-drive limit

While the Γ_{L} dependence of the photocurrent is explained above, the photocurrent oscillations require additional analysis. To that aim, we focus on the large-drive

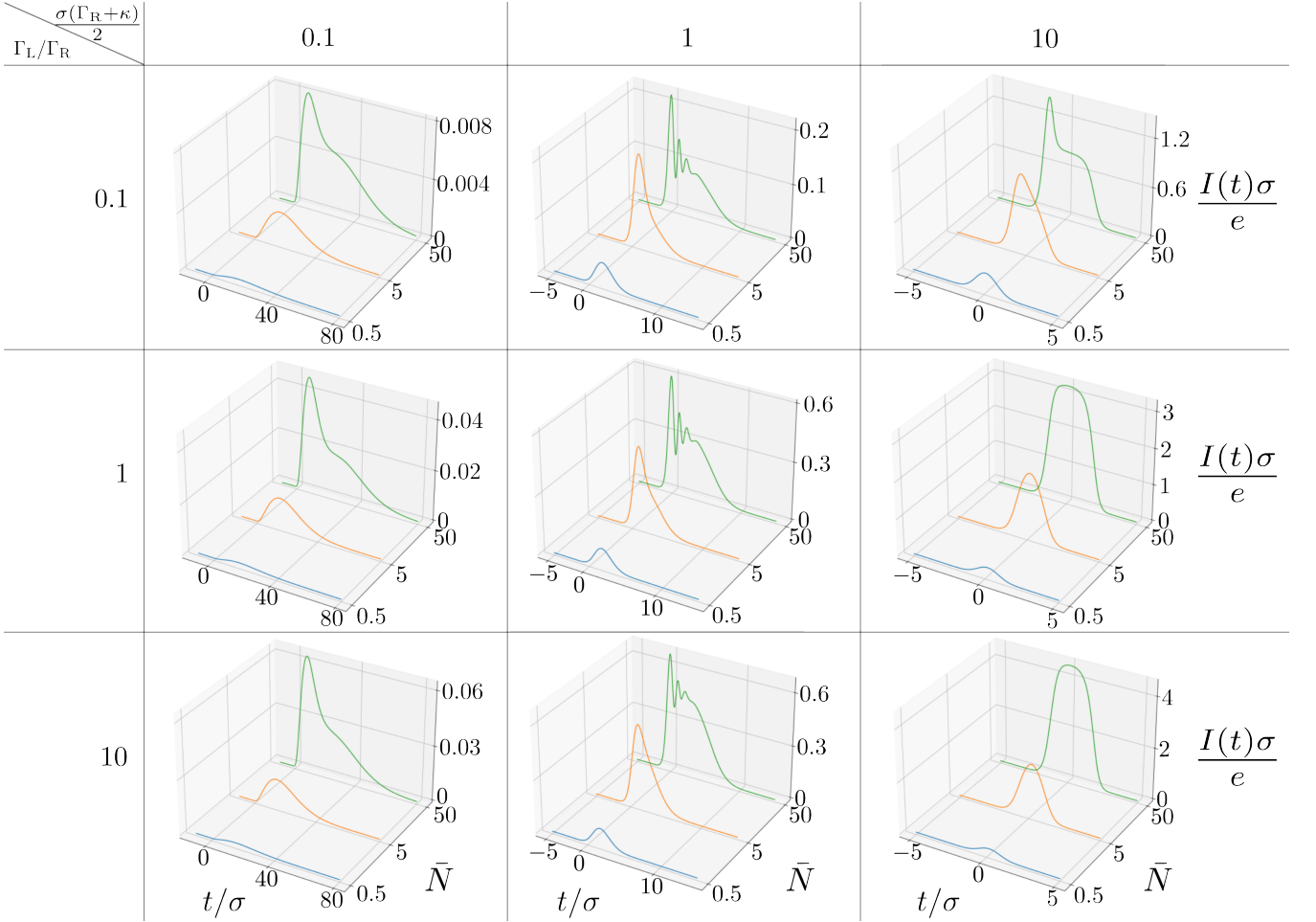


FIG. 7. Normalized photocurrent as a function of time and average number of photons in the Gaussian drive for $\sigma(\Gamma_R + \kappa)/2 = 0.1, 1, \text{ and } 10$, $\Gamma_L/\Gamma_R = 0.1, 1, \text{ and } 10$, and $\bar{N} = 0.5, 5, \text{ and } 50$.

limit, $\bar{N} \gg 1$, where the influence of the DQD on the resonator field can be neglected and the photon operators a, a^\dagger can be taken equal to their average values, $\langle a \rangle, \langle a^\dagger \rangle$. The time evolution of the average $\langle a \rangle(t)$ is given by the equation

$$\partial_t \langle a \rangle(t) = -\frac{\kappa}{2} \langle a \rangle(t) - i\sqrt{\kappa} f(t), \quad (36)$$

where we recall that $f(t)$ is the time dependent drive amplitude. Following our earlier work, [27], we can then write the equations of motion for the DQD density matrix components as

$$\partial_t p_0(t) = -\Gamma_L p_0(t) + \Gamma_R p_e(t), \quad (37)$$

$$\begin{aligned} \partial_t p_e(t) = & -\Gamma_R p_e(t) \\ & -ig [\langle a \rangle(t) \langle \sigma_+ \rangle(t) - \langle a^\dagger \rangle(t) \langle \sigma_- \rangle(t)], \end{aligned} \quad (38)$$

$$\begin{aligned} \partial_t p_g(t) = & \Gamma_L p_0(t) \\ & +ig [\langle a \rangle(t) \langle \sigma_+ \rangle(t) - \langle a^\dagger \rangle(t) \langle \sigma_- \rangle(t)], \end{aligned} \quad (39)$$

$$\partial_t \langle \sigma_- \rangle(t) = -\frac{\Gamma_R}{2} \langle \sigma_- \rangle(t) + ig \langle a \rangle(t) [p_e(t) - p_g(t)], \quad (40)$$

where the probabilities $p_\alpha(t) = \langle \alpha | \rho | \alpha \rangle$, $\alpha = 0, e, g$, with $p_e(t) + p_g(t) + p_0(t) = 1$, and $\langle \sigma_- \rangle(t) = \langle e | \rho | g \rangle = [\langle \sigma_+ \rangle(t)]^*$. From the density matrix components, the photocurrent can be calculated via Eq. (5).

To illustrate that these equations correctly describe the photocurrent in the large-drive limit, we compare their solution to the exact numerical solution for a Gaussian pulse, see Fig. 8.

As is clear from the figure, the large-drive equations capture the time dependence of the photocurrent well, including the Γ_L dependence and the temporal oscillations.

To obtain a simple picture of the oscillations we further consider the limit where Γ_L is much larger than Γ_R . In this limit the DQD is rapidly refilled when an electron tunnels out, which implies that the DQD is essentially never empty, $p_0(t) \ll 1$. We can then, to leading order in Γ_R/Γ_L , perform an adiabatic elimination of $p_0(t)$ from

Eq. (37), resulting in $p_0(t) = \Gamma_R/\Gamma_L p_e(t)$. Inserting this back into the remaining equations we get

$$\begin{aligned} \partial_t p_e(t) &= -\Gamma_R p_e(t) - i[\Omega^*(t)\langle\sigma_+\rangle(t) - \Omega(t)\langle\sigma_-\rangle(t)], \\ \partial_t p_g(t) &= \Gamma_R p_e(t) + i[\Omega^*(t)\langle\sigma_+\rangle(t) - \Omega(t)\langle\sigma_-\rangle(t)], \\ \partial_t \langle\sigma_-\rangle(t) &= -\frac{\Gamma_R}{2}\langle\sigma_-\rangle(t) + i\Omega^*(t)[p_e(t) - p_g(t)], \end{aligned} \quad (41)$$

where we introduced $\Omega(t) = g\langle a^\dagger \rangle(t)$. The equations in (41) are the well known equations for the semiclassical Rabi problem [61, 62], describing a driven two-level system with a decay rate Γ_R . Here we consider a drive with a time dependent amplitude, giving rise to a time dependent Rabi frequency $\Omega(t)$.

The temporal oscillations in the photocurrent, visible in Figs. 7 and 8, can thus be understood as manifestations of the coherent excitation and de-excitation of the DQD, induced by the photon pulse and decaying with time due to the tunneling out of the electron from the DQD. The effect of the time dependence of the Rabi frequency is primarily to modulate the frequency of the photocurrent oscillations.

Further insight can be obtained by considering the regime of weak decay, $\Gamma_R \ll \kappa$, analyzing the different temporal regimes. For times much shorter than the decay time, $t \ll 1/\Gamma_R$, the photocurrent is given from the so-called area law [63], as

$$I(t)/e = \Gamma_R \sin^2[\mathcal{A}(t)], \quad \mathcal{A}(t) = \int_{-\infty}^t dt' \Omega(t'). \quad (42)$$

The photocurrent thus displays modulated oscillations with a time-dependent frequency. For times much longer than the decay time of photons in the resonator, $t \gg 1/\kappa$, the resonator is empty, $\langle a(t) \rangle = 0$, and hence $\Omega(t) = 0$. In this regime, it follows directly from Eq. (41) that $p_e(t) \sim e^{-t\Gamma_R}$, exponentially decaying in time. Based on these two limiting cases, we can obtain an approximate expression for the photocurrent for all times, including the regime $1/\Gamma_R < t < 1/\kappa$ where none of the limiting expressions are formally valid. To do this, we apply boundary-layer theory [64], matching the asymptotics of the two expressions. This gives the photocurrent, see Appendix D, as

$$I(t)/e = \Gamma_R \sin^2[\mathcal{A}(t)] e^{-t\Gamma_R}. \quad (43)$$

This expression captures both the temporal oscillations and the exponential decay and approximates well the exact result, as illustrated in Fig. 8.

In addition, we note that an analytical treatment is amenable for a very short drive pulse, taking $f(t) = A\delta(t)$, a δ -function with strength A . This leads, via Eq. (36), to a Rabi frequency $\Omega(t) = -ig\sqrt{\kappa}Ae^{-t\kappa/2}\Theta(t)$,

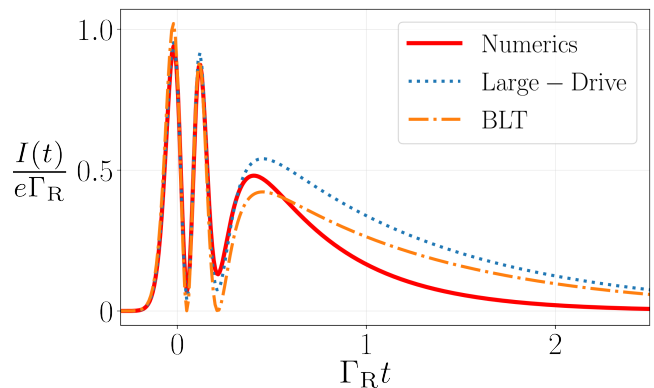


FIG. 8. Photocurrent from the full numerics (full line), the large-drive limit (dotted line), and the boundary-layer theory (dashed-dotted line) with $\bar{N} = 150$, $\sigma\Gamma_R = 0.1$, $\kappa/\Gamma_R = 20$, $\Gamma_L/\Gamma_R = 12$ and $t_c/\Gamma_R = \gamma_-/\Gamma_R = \gamma_\phi/\Gamma_R = 0$.

displaying a sharp onset of amplitude $g\sqrt{\kappa}A$ at $t = 0$, followed by an exponential decay with rate $\kappa/2$. Inserting this into the Rabi equations (41), the resulting system of differential equations can be solved analytically. The resulting expression for the photocurrent $I(t)/e = \Gamma_R p_e(t)$ is however lengthy and provides little qualitative insight and is therefore only presented, together with the derivation, in Appendix E.

B. Detection efficiency

Out of the three detector performance quantifiers analyzed in the low-drive limit, the detection efficiency is the most interesting one to investigate beyond low drive - the strongly modified temporal properties of the photocurrent make the delay time and fidelity less relevant. The photodetection efficiency for both a Gaussian and a Lorentzian drive pulse are shown in Fig. 9 for a representative set of system parameters. From the figure it is clear that the overall trend is a suppressed efficiency for increasing drive strength. However, for a wide pulse, $\sigma(\Gamma_R + \kappa) \gg 1$, the efficiency remains close to unity also for large $\bar{N} \gg 1$. In this regime the detector successively, and efficiently, converts individual pulse photons into electrons traversing the DQD.

VI. CONCLUSIONS AND OUTLOOK

To summarize, we have theoretically investigated the detection of single microwave pulses in a resonator-coupled DQD. In the regime of low applied drive, the drive and detector can be described in terms of Wigner functions, which allows for a clear and visually com-

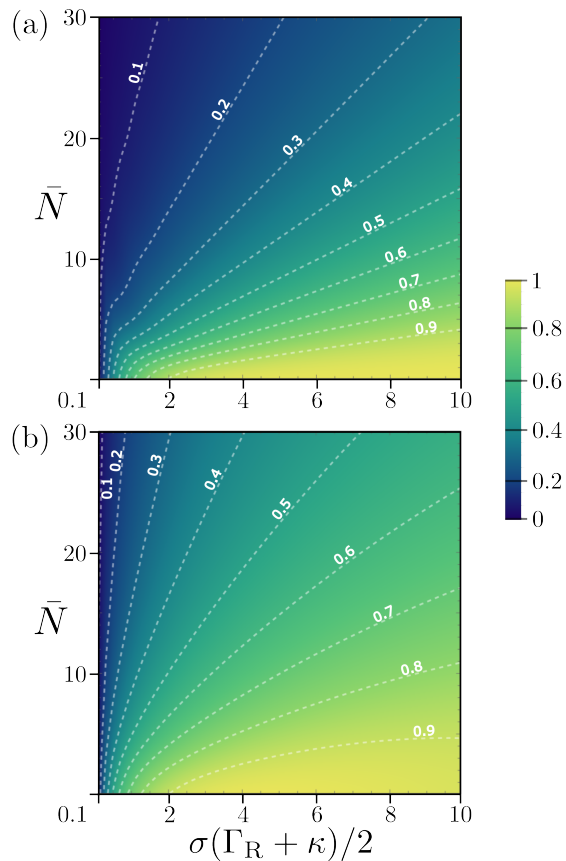


FIG. 9. Photodetection efficiency as a function of \bar{N} and $\sigma(\Gamma_R + \kappa)/2$ with $\Gamma_R/\kappa = 1$ and $\Gamma_L/\Gamma_R = 1$, for (a) a Gaussian drive and (b) a Lorentzian drive.

elling analysis of their time and frequency dependence. This Wigner-function description was used to compute the outgoing photocurrent pulse, which was compared to the incoming microwave pulse in different parameter regimes. In the regime of a broadband photodetector, the performance of the detector was found to be almost ideal.

Moving away from the low-drive limit, we observed oscillations in the photocurrent, which we attribute to Rabi oscillations. We have also found an approximate and compelling analytical solution for the large-drive photocurrent by employing boundary-layer theory, capturing the qualitative behavior of the exact numerical solutions for the photocurrent.

Our results pave the way for a better theoretical understanding of single microwave pulse photodetection inside a DQD-resonator system and could inspire future experiments in this avenue. On the theoretical side, expressing the photodetection as a Volterra series may enable an analytic understanding of photodetection beyond weak drives. In addition, the development of a Wigner-function formalism for the outgoing photocurrent pulse may shed further insight into the photodetection process. Other intriguing avenues for research include examining different types of drives, such as non-classical states of light, as well as the potential to generate said states and investigate their statistical properties [65–68].

ACKNOWLEDGMENTS

This work was supported by the Knut and Alice Wallenberg Foundation through the Wallenberg Center for Quantum Technology (WACQT). P.P.P. acknowledges funding from the Swiss National Science Foundation (Eccellenza Professorial Fellowship PCEFP2_194268).

Appendix A: Photocurrent in the low-drive limit

To compute the photocurrent in Eq. (5), we need to find the occupations of the excited state p_e and the empty state p_0 . These quantities are found using the master equation (4) together with the equality $\langle x \rangle = \text{Tr}\{x\rho(t)\}$. This leads to a set of coupled equations of motion. Expanding this set of equations to lowest order in the drive gives

$$\partial_t p_0(t) = -\Gamma_{g0} p_0(t) + \Gamma_{0e} p_e(t), \quad (\text{A1})$$

$$\partial_t p_e(t) = -(\Gamma_{0e} + \gamma_-) p_e(t) + 2g \text{Im} \langle a \sigma_+ \rangle (t), \quad (\text{A2})$$

$$\partial_t \text{Im} \langle a \sigma_+ \rangle (t) = -\frac{1}{2} (\tilde{\Gamma} + \kappa) \text{Im} \langle a \sigma_+ \rangle (t) - g p_e(t) - \frac{\sqrt{\kappa_{\text{in}}}}{2} [f^*(t) \langle \sigma_+ \rangle (t) + f(t) \langle \sigma_- \rangle (t)] + g \langle a^\dagger a \rangle (t), \quad (\text{A3})$$

$$\partial_t \langle \sigma_- \rangle (t) = -\frac{\tilde{\Gamma}}{2} \langle \sigma_- \rangle (t) - ig \langle a \rangle (t), \quad (\text{A4})$$

$$\partial_t \langle a \rangle (t) = -\frac{\kappa}{2} \langle a \rangle (t) - i\sqrt{\kappa_{\text{in}}} f^*(t) - ig \langle \sigma_- \rangle (t), \quad (\text{A5})$$

$$\partial_t \langle a^\dagger a \rangle (t) = -\kappa \langle a^\dagger a \rangle (t) - 2g \text{Im} \langle a \sigma_+ \rangle (t) + i\sqrt{\kappa_{\text{in}}} [f(t) \langle a \rangle (t) - f^*(t) \langle a^\dagger \rangle (t)]. \quad (\text{A6})$$

The equations are most readily solved in Fourier space. In what follows, we use these definitions for the Fourier transform

$$\tilde{f}(\omega) = \frac{1}{\sqrt{2\pi}} \int dt f(t) e^{i\omega t}, \quad \tilde{f}(\omega, \omega') = \frac{1}{2\pi} \int dt dt' f(t, t') e^{i(\omega t + \omega' t')}. \quad (\text{A7})$$

The photocurrent is then found to be of the following form

$$\tilde{I}(\omega)/e = \frac{1}{\sqrt{2\pi}} \int \frac{d\omega'}{2\pi} \tilde{h}(\omega - \omega', \omega') \tilde{f}(\omega - \omega') \tilde{f}^*(\omega'), \quad (\text{A8})$$

where $\tilde{f}^*(\omega)$ is the Fourier transform of $f^*(t)$ and $\tilde{h}(\omega, \omega') = \tilde{g}(\omega, \omega') + \tilde{g}(\omega', \omega)$, with

$$\tilde{g}(\omega, \omega') = \frac{16\pi g^2 \kappa_{\text{in}} [-\tilde{\Gamma} + \kappa + i(\omega + 3\omega')]}{[\Gamma_{g0} - i(\omega + \omega')][4g^2 + (\tilde{\Gamma} - 2i\omega')(\kappa - 2i\omega')]\Lambda}, \quad (\text{A9})$$

where

$$\Lambda = 4g^2 [\Gamma_{0e} + \gamma_- + \kappa - 2i(\omega + \omega')] + [\tilde{\Gamma} + \kappa - 2i(\omega + \omega')][(\Gamma_{0e} + \gamma_- - i(\omega + \omega'))[\kappa - i(\omega + \omega')]]. \quad (\text{A10})$$

In the ideal-detector limit, Eq. (A9) becomes

$$\tilde{g}(\omega, \omega') = \frac{2\pi \Gamma_{\text{R}}^2 \kappa^2 [\Gamma_{\text{R}} + \kappa - i(\omega + 3\omega')]}{[\Gamma_{\text{R}} + \kappa - 2i(\omega + \omega')][\Gamma_{\text{R}} \kappa - i\omega'(\Gamma_{\text{R}} + \kappa) - 2\omega'^2] \{2\Gamma_{\text{R}} \kappa - i(\omega + \omega')[\Gamma_{\text{R}} + \kappa - i(\omega + \omega')]\}}. \quad (\text{A11})$$

Taking the Fourier transform of Eq. (A8) and replacing $\omega \rightarrow \omega + \omega'$, we get

$$I(t)/e = \frac{1}{(2\pi)^2} \int d\omega d\omega' e^{-i(\omega + \omega')t} \tilde{h}(\omega, \omega') \tilde{f}(\omega) \tilde{f}^*(\omega') = \frac{1}{2\pi} \int_0^\infty d\tau d\tau' h(\tau, \tau') f(t - \tau) f^*(t - \tau'), \quad (\text{A12})$$

where $h(\tau, \tau')$ is the Fourier transform of $\tilde{h}(\omega, \omega')$. We note that $h(\tau, \tau') = h(\tau', \tau)$. The integral in Eq. (A12) only runs over positive times. This is because the function $\tilde{g}(\omega, \omega')$ in Eq. (A9) only has poles in the lower half plane, which results in $h(\tau, \tau')$ vanishing at negative times. We also note that $\tilde{h}(\omega, \omega') = \tilde{h}^*(-\omega, -\omega')$, and thus $h(\tau, \tau') = h^*(\tau, \tau')$. We now have all the tools to introduce the Wigner function for the detector

$$W_{\text{d}}(t, \omega) = \frac{1}{2\pi} \int d\xi e^{-i\xi\omega} h(t + \xi/2, t - \xi/2) = \frac{1}{2\pi} \int d\chi e^{i\chi t} \tilde{h}(\omega + \chi/2, \omega - \chi/2), \quad (\text{A13})$$

In addition, we define a Wigner function for the drive

$$W_{\text{f}}(t, \omega) = \frac{1}{2\pi} \int d\xi e^{-i\xi\omega} f(t + \xi/2) f^*(t - \xi/2). \quad (\text{A14})$$

This allows us to write the photocurrent as

$$I(t)/e = \int d\tau d\omega W_{\text{d}}(\tau, \omega) W_{\text{f}}(t - \tau, \omega). \quad (\text{A15})$$

Appendix B: Photocurrent expressions in the ideal-detector limit

In the frequency domain, we find an analytical expression for the photocurrent in the ideal-detector limit when the system is driven by a Gaussian pulse by plugging Eq. (13) into Eq. (A8). We find

$$\tilde{I}(\omega)/e = \frac{\sqrt{\pi}\bar{N}\Gamma_R^2\kappa^2\sigma e^{-\frac{\sigma^2[(2\omega-iy)^2+4\omega^2]}{16}} \left\{ e^{\frac{i\alpha\sigma^2(\Gamma_R+\kappa-2i\omega)}{4}} (iy+2\omega)\text{erfc}\left[\frac{\sigma(x-2i\omega)}{4}\right] - (ix+2\omega)\text{erfc}\left[\frac{\sigma(y+2i\omega)}{4}\right] \right\}}{\alpha(\Gamma_R+\kappa-2i\omega)[2\Gamma_R\kappa-i\omega(\Gamma_R+\kappa)-\omega^2]}, \quad (\text{B1})$$

where $x = \Gamma_R + \kappa + i\alpha$, $y = \Gamma_R + \kappa - i\alpha$ and $\text{erfc}(z)$ gives the complementary error function. For the case of a Lorentzian pulse drive, we plug Eq. (16) into Eq. (A8) and find

$$\begin{aligned} \tilde{I}(\omega)/e = & \frac{\bar{N}\Gamma_R^2\kappa^2\sigma}{\alpha(\Gamma_R+\kappa-2i\omega)[2\Gamma_R\kappa-i\omega(\Gamma_R+\kappa)-\omega^2]} \\ & \times \left\{ e^{\frac{\sigma}{2}(iy+2\omega)(x-2i\omega)} \left\{ \Gamma(0, \sigma(iy+2\omega)/2) - [\Gamma(0, \sigma(iy+2\omega)/2) - \Gamma(0, i\sigma y/2)]\Theta(-\omega) \right\} \right. \\ & - e^{-\frac{\sigma}{2}(iy+2\omega)(x-2i\omega)} \left\{ \Gamma(0, -\sigma(iy+2\omega)/2) - [\Gamma(0, -\sigma(iy+2\omega)/2) - \Gamma(0, -i\sigma y/2)]\Theta(\omega) \right\} \\ & - e^{\frac{\sigma}{2}(ix+2\omega)(y-2i\omega)} \left\{ \Gamma(0, \sigma(ix+2\omega)/2) + [\Gamma(0, i\sigma x/2) - \Gamma(0, \sigma(ix+2\omega)/2)]\Theta(-\omega) \right. \\ & \left. \left. - e^{-\sigma(ix+2\omega)} \left\{ \Gamma(0, -\sigma(ix+2\omega)/2) - [\Gamma(0, -\sigma(ix+2\omega)/2) - \Gamma(0, -i\sigma x/2)]\Theta(\omega) \right\} \right\} \right\}, \quad (\text{B2}) \end{aligned}$$

where $\Gamma(a, z)$ is the incomplete Gamma function. The time-dependent photocurrent in Fig. 4 is then found by inverse Fourier transformation.

Appendix C: Properties of the Wigner functions

In this appendix, we derive properties of the Wigner function including the bound on its absolute value in Eq. (28) as well as the time-energy uncertainty relation in Eq. (26). To this end, we are going to use analogies to the phase space Wigner function used in quantum mechanics making use of the following properties of the function $h(\tau, \tau')$ that are proven in Appendix A

$$h(\tau, \tau') = h(\tau', \tau), \quad h^*(\tau, \tau') = h(\tau, \tau'). \quad (\text{C1})$$

1. Analogy to phase space Wigner function

We may interpret h as an operator on the vector space of square-integrable functions acting on a function $u(\tau)$ as

$$(hu)(\tau) \equiv \int d\tau' h(\tau, \tau')u(\tau'). \quad (\text{C2})$$

The inner product on this space is defined in the usual manner

$$\langle v, u \rangle = \int d\tau v^*(\tau)u(\tau). \quad (\text{C3})$$

With Eqs. (C1)-(C3), one may show that

$$\langle v, hu \rangle = \langle hv, u \rangle, \quad (\text{C4})$$

implying that h is a Hermitian operator. We now introduce the normalized function

$$\bar{h}(\tau, \tau') = \frac{h(\tau, \tau')}{\int dx h(x, x)}. \quad (\text{C5})$$

We may use the spectral theorem to write

$$\bar{h}(\tau, \tau') = \sum_j p_j u_j(\tau)u_j^*(\tau'), \quad (\text{C6})$$

where u_j denote the orthonormal eigenvectors of h , i.e.,

$$\int d\tau' \bar{h}(\tau, \tau')u_j(\tau') = p_j u_j(\tau), \quad (\text{C7})$$

with

$$\int d\tau u_j^*(\tau)u_k(\tau) = \delta_{j,k}. \quad (\text{C8})$$

The normalization in Eq. (C5) ensures that \bar{h} has unit trace, i.e.,

$$\sum_j p_j = 1. \quad (\text{C9})$$

We note that there is an analogy between $\bar{h}(\tau, \tau')$ and the elements of a density matrix in quantum mechanics, which can be written as

$$\langle x|\hat{\rho}|x' \rangle = \rho(x, x') = \sum_j p_j \psi_j(x)\psi_j^*(x'). \quad (\text{C10})$$

To make the analogy complete, we need to require that $p_j \geq 0$. This is ensured by assuming that $h(\tau, \tau')$ is a

positive semi-definite function. From Eq. (7), we may infer that this is equivalent to assuming that the photocurrent $I(t)/e$ is non-negative at all times and for all drive amplitudes. To see this, we note that $h(\tau, \tau') = 0$ if either $\tau < 0$ or $\tau' < 0$. Equation (7) may thus be written as

$$I(t)/e = \int d\tau d\tau' s^*(\tau) \bar{h}(\tau, \tau') s(\tau') \geq 0, \quad (\text{C11})$$

with $s(\tau) = \sqrt{\int dx h(x, x)} f^*(t - \tau) / \sqrt{2\pi}$, which is the defining property of a positive semi-definite function. We note that for our detector, the current may become negative due to back-tunneling from the drain lead. The properties discussed in this appendix cannot be applied to this scenario.

With the analogy between \bar{h} and a quantum-mechanical density matrix at hand, we may use standard properties of quantum-mechanical Wigner functions. We focus on two properties. First, we provide a bound on maximal and minimal values for h , and second, we prove the Heisenberg-Gabor limit in analogy to the Heisenberg uncertainty relation.

2. Bounding the Wigner function

With the results of the last section, we may prove Eq. (28) in complete analogy to the bound on the phase-space Wigner function, see for instance Ref. [69]

$$\begin{aligned} \frac{|W(t, \omega)|}{\bar{W}_d} &= \frac{1}{2\pi} \left| \int_{-\infty}^{\infty} d\xi e^{-i\xi\omega} \bar{h}(t + \xi/2, t - \xi/2) \right| \\ &= \frac{1}{2\pi} \left| \sum_j p_j \int_{-\infty}^{\infty} d\xi e^{-i\xi\omega} u_j(t + \xi/2) u_j^*(t - \xi/2) \right| \\ &= \frac{1}{2\pi} \left| \sum_j p_j \langle u_j^*(t - \xi/2), e^{-i\xi\omega} u_j(t + \xi/2) \rangle \right| \\ &\leq \frac{1}{2\pi} \sum_j p_j |\langle u_j^*(t - \xi/2), e^{-i\xi\omega} u_j(t + \xi/2) \rangle| \\ &\leq \frac{1}{2\pi} \sum_j p_j \langle u_j(\xi/2), u_j(\xi/2) \rangle \\ &= \frac{1}{\pi}. \end{aligned} \quad (\text{C12})$$

Here the first inequality is simply the triangle inequality, while the second inequality is the Cauchy-Schwarz inequality. In addition, we used the identities

$$\langle e^{i\varphi} f, e^{i\varphi} g \rangle = \langle f, g \rangle, \quad (\text{C13})$$

for any $\varphi \in \mathbb{R}$, and

$$\langle u_j(t \pm \xi/2), u_j(t \pm \xi/2) \rangle = \langle u_j(\xi/2), u_j(\xi/2) \rangle, \quad (\text{C14})$$

where the inner product is understood to be over the variable ξ .

3. The Heisenberg-Gabor limit

To prove the Heisenberg-Gabor limit [57] in Eq. (26), we introduce the moments of the normalized Wigner function as

$$\langle x \rangle = \int dt d\omega x W_d(t, \omega) / \bar{W}_d. \quad (\text{C15})$$

From Eq. (C6) we may infer that $\langle x \rangle = \sum_j p_j \langle x \rangle_j$. We thus find

$$\begin{aligned} \Delta t \Delta \omega &= \sqrt{\sum_j p_j \langle (t - \langle t \rangle)^2 \rangle_j \sum_k p_k \langle (\omega - \langle \omega \rangle)^2 \rangle_k} \\ &\geq \sum_j p_j \sqrt{\langle (t - \langle t \rangle)^2 \rangle_j \langle (\omega - \langle \omega \rangle)^2 \rangle_j}, \end{aligned} \quad (\text{C16})$$

where we employed the Cauchy-Schwarz inequality. Next we write

$$\begin{aligned} \langle (t - \langle t \rangle)^2 \rangle_j &= \int dt u_j^*(t) (t - \langle t \rangle)^2 u_j(t) \\ &= \langle (t - \langle t \rangle) u_j(t), (t - \langle t \rangle) u_j(t) \rangle, \end{aligned} \quad (\text{C17})$$

where we note the difference between the averages $\langle x \rangle$ and $\langle f, g \rangle$, which are defined in Eqs. (C15) and (C3) respectively.

Similarly to how the momentum operator can be written as a derivative of position, we may obtain the frequency moments using time derivatives as

$$\begin{aligned} \langle (\omega - \langle \omega \rangle)^2 \rangle_j &= \int dt u_j^*(t) (-i\partial_t - \langle \omega \rangle)^2 u_j(t) \\ &= \langle (-i\partial_t - \langle \omega \rangle) u_j(t), (-i\partial_t - \langle \omega \rangle) u_j(t) \rangle, \end{aligned} \quad (\text{C18})$$

where the first equality can be derived from Eq. (A13) and the last equality can be proven using integration by parts. We may now use the Cauchy-Schwarz inequality to write

$$\sqrt{\langle r(t), r(t) \rangle \langle s(t), s(t) \rangle} \geq |\langle r(t), s(t) \rangle| \geq |\text{Im}\{\langle r(t), s(t) \rangle\}|. \quad (\text{C19})$$

With $r(t) = (t - \langle t \rangle) u_j(t)$ and $s(t) = (-i\partial_t - \langle \omega \rangle) u_j(t)$, we find

$$\sqrt{\langle (t - \langle t \rangle)^2 \rangle_j \langle (\omega - \langle \omega \rangle)^2 \rangle_j} \geq \frac{1}{2}, \quad (\text{C20})$$

where we again used integration by parts. Inserting the last inequality into Eq. (C16), we recover the Heisenberg-Gabor limit in Eq. (26).

Appendix D: Approximate solution, boundary-layer theory

Here we discuss the derivation of the boundary-layer theory (BLT) approximation for the photocurrent, c.f. Eq. (43). The starting point is the Rabi equations in Eq. (41) for the DQD density matrix components, keeping in mind that the photocurrent is given by $I(t) = e\Gamma_R p_e(t)$. Note that the difference from the photocurrent introduced in Eq. (5) is due to the small interdot tunneling requirement in Tab. I, which leads to $\theta \rightarrow 0$. As pointed out in the main text, at times much shorter than the inverse decay rate, $t \ll 1/\Gamma_R$, the DQD evolution is fully coherent and the photocurrent is given by the area law expression in Eq. (42),

$$I_{\text{in}}(t) = e\Gamma_R \sin^2[\mathcal{A}(t)], \quad \mathcal{A}(t) = \int_{-\infty}^t dt' \Omega(t'). \quad (\text{D1})$$

where we here introduced the subscript “in”, denoting the *inner* solution according to the nomenclature of BLT.

Focusing on the regime of weak decay, $\Gamma_R \ll \kappa$, in the limit of times much longer than the resonator photon decay time, $t \gg 1/\kappa$, the resonator is empty. As pointed out in the main text, the photocurrent is then given directly via the equation for $p_e(t)$ in Eq. (41), as

$$I_{\text{out}}(t) = ce\Gamma_R e^{-t\Gamma_R}, \quad (\text{D2})$$

where c is a constant and we added the subscript “out”, denoting the *outer* solution. In order to obtain the BLT expression for the photocurrent, describing also times $1/\kappa < t < 1/\Gamma_R$, the first step is to determine the constant c by requiring that the asymptotic photocurrent expressions are equal, as (assuming a pulse that starts around $t = 0$)

$$I_{\text{in}}(\infty) = I_{\text{out}}(0) \quad \Rightarrow \quad c = \sin^2[\mathcal{A}(\infty)]. \quad (\text{D3})$$

As a second step, an approximate, BLT photocurrent expression is obtained by adding the inner and outer so-

lutions and then subtracting their common asymptotic value, as

$$\begin{aligned} I_{\text{BLT}}(t) &= I_{\text{in}}(t) + I_{\text{out}}(t) - e\Gamma_R \sin^2[\mathcal{A}(\infty)] \\ &= e\Gamma_R \left\{ \sin^2[\mathcal{A}(t)] + \sin^2[\mathcal{A}(\infty)] (e^{-t\Gamma_R} - 1) \right\}, \end{aligned} \quad (\text{D4})$$

Finally, by writing the expression in the curly brackets in Eq. (D5) as $\sin^2[\mathcal{A}(t)] e^{-t\Gamma_R} + \{\sin^2[\mathcal{A}(\infty)] - \sin^2[\mathcal{A}(t)]\} (e^{-t\Gamma_R} - 1)$, we see that the second term in this expression is much smaller than the first one for all relevant t and can thus simply be dropped. This then gives the photocurrent

$$I_{\text{BLT}}(t) = e\Gamma_R \sin^2[\mathcal{A}(t)] e^{-t\Gamma_R}, \quad (\text{D5})$$

which is the expression presented in Eq. (43) in the main text.

Appendix E: Exact result, impulse response

Here we present the derivation of the formal solution for the Rabi equations in Eq. (41) for a δ -function pulse, i.e., the impulse response $f(t) = A\delta(t)$, with A being a real constant. As a starting point, using Eq. (36) for the resonator amplitude $\langle a \rangle(t)$ with the initial condition $\langle a \rangle(-\infty) = 0$, a δ -function input gives

$$\langle a \rangle(t) = -i\sqrt{\kappa} A e^{-\kappa t/2}, \quad t \geq 0. \quad (\text{E1})$$

The amplitude is purely imaginary, $\langle a^\dagger \rangle(t) = -\langle a \rangle(t)$, and exponentially decaying with time after a step onset at $t = 0$. Accounting for the imaginary $\langle a \rangle(t)$ and making use of the normalization $p_e(t) + p_g(t) = 1$, we can reduce the Rabi equations to two coupled linear differential equations for $p_e(t)$ and $\langle \sigma_x \rangle(t) = \langle \sigma_- + \sigma_+ \rangle(t)$, as

$$\begin{aligned} \partial_t p_e(t) &= -\Gamma_R p_e(t) - ig\langle a \rangle(t) \sigma_x(t), \\ \partial_t \langle \sigma_x \rangle(t) &= -\frac{\Gamma_R}{2} \langle \sigma_x \rangle(t) + ig\langle a \rangle(t) [2p_e(t) - 1], \end{aligned} \quad (\text{E2})$$

here writing out $\Omega(t) = -\Omega^*(t) = -g\langle a \rangle(t)$ for clarity. To obtain an equation for $p_e(t)$ only, we take the derivative of the first equation in Eq. (E2) and then insert the expression for $\partial_t \langle \sigma_x \rangle(t)$ from the second equation and $\langle \sigma_x \rangle(t) = i[\Gamma p_e(t) + \dot{p}_e(t)]/g$ from the first, giving

$$\partial_t^2 p_e(t) = -\left[\frac{3\Gamma_R}{2} - \frac{\langle \dot{a} \rangle(t)}{\langle a \rangle(t)} \right] \dot{p}_e(t) - \Gamma_R \left[\frac{\Gamma_R}{2} - \frac{\langle \dot{a} \rangle(t)}{\langle a \rangle(t)} \right] p_e(t) + g^2 \langle a \rangle^2(t) [2p_e(t) - 1]. \quad (\text{E3})$$

Inserting the expression for $\langle a \rangle(t)$ in Eq. (E1), making use of that $\langle \dot{a} \rangle(t)/\langle a \rangle = -\kappa/2$ and rearranging, we can write the equation for $p_e(t)$ in the form

$$\partial_t^2 p_e(t) + \frac{3\Gamma_R + \kappa}{2} \dot{p}_e(t) + \left[\frac{\Gamma_R(\Gamma_R + \kappa)}{2} + 4g^2 \kappa A^2 e^{-t\kappa} \right] p_e(t) = 2g^2 \kappa A^2 e^{-t\kappa}. \quad (\text{E4})$$

To proceed, we write $p_e(t) = y(t)e^{-(3\Gamma_R + \kappa)t/4}$ and change variables as $x = 4gAe^{-\kappa t/2}/\sqrt{\kappa}$, giving the equation for $y(x)$ as

$$x^2 \frac{d^2 y(x)}{dx^2} + x \frac{dy(x)}{dx} + (x^2 - \nu^2)y(x) = \mu^{2+3\nu} x^{-3\nu}, \quad (\text{E5})$$

where we introduced $\nu = (\Gamma_R/\kappa - 1)/2$ and $\mu = 4gA/\sqrt{\kappa}$. We note that putting the right hand side equal to zero, the resulting homogenous equation is Bessel's equation, with solutions $J_\nu(x)$ and $Y_\nu(x)$. The general solution is given by the sum of the homogenous solution, $y_h(x) = C_1 J_\nu(x) + C_2 Y_\nu(x)$ with C_1, C_2 constants, and a particular solution

$$y_p(x) = \frac{\pi}{2} \mu^{2+3\nu} J_\nu(x) \int dx Y_\nu(x) x^{1-3\nu} - \frac{\pi}{2} \mu^{2+3\nu} Y_\nu(x) \int dx J_\nu(x) x^{1-3\nu}, \quad (\text{E6})$$

where we have used that the Wronskian $(dY_\nu(x)/dx)J_\nu(x) - (dJ_\nu(x)/dx)Y_\nu(x) = 2/(\pi x)$. Performing the integrals and implementing the initial conditions $y(\mu) = dy(x)/dx|_{x=\mu} = 0$, the full solution for $y(x)$ can be written in the arguably not very transparent way, as

$$y(x) = \frac{\pi 2^{-3+\nu} \mu^{2-\nu} x^{-4\nu} J_\nu(x) \csc(\pi\nu)}{\nu^2 \Gamma(-\nu)} \left[\mu^{4\nu} {}_1F_2 \left(-2\nu; 1-2\nu, 1-\nu; -\frac{x^2}{4} \right) - x^{4\nu} {}_1F_2 \left(-2\nu; 1-2\nu, 1-\nu; -\frac{\mu^2}{4} \right) \right] + \frac{2^{-2-\nu} \mu^{2+\nu} x^{-2\nu} J_{-\nu}(x) \Gamma(-\nu)}{\nu} \left[x^{2\nu} {}_1F_2 \left(-\nu; 1-\nu, 1+\nu; -\frac{\mu^2}{4} \right) - \mu^{2\nu} {}_1F_2 \left(-\nu; 1-\nu, 1+\nu; -\frac{x^2}{4} \right) \right], \quad (\text{E7})$$

where ${}_pF_q$ is the hypergeometric function and Γ the Gamma function. From above we then have

$$p_e(t) = e^{-(3\Gamma_R + \kappa)t/4} y(4gAe^{-\kappa t/2}/\sqrt{\kappa}). \quad (\text{E8})$$

-
- [1] M. D. Eisaman, J. Fan, A. Migdall, and S. V. Polyakov, "Invited review article: Single-photon sources and detectors," *Rev. Sci. Instrum.* **82**, 071101 (2011).
- [2] S. Pirandola, U. L. Andersen, L. Banchi, M. Berta, D. Bunandar, R. Colbeck, D. Englund, T. Gehring, C. Lupo, C. Ottaviani, J. L. Pereira, M. Razavi, J. S. Shaari, M. Tomamichel, V. C. Usenko, G. Vallone, P. Villoresi, and P. Wallden, "Advances in quantum cryptography," *Adv. Opt. Photon.* **12**, 1012–1236 (2020).
- [3] M. Herrero-Collantes and J. C. Garcia-Escartin, "Quantum random number generators," *Rev. Mod. Phys.* **89**, 015004 (2017).
- [4] E. Knill, R. Laflamme, and G. J. Milburn, "A scheme for efficient quantum computation with linear optics," *Nature* **409**, 46 (2001).
- [5] W. Pernice, C. Schuck, O. Minaeva, M. Li, G. Goltsman, A. Sergienko, and H. Tang, "High-speed and high-efficiency travelling wave single-photon detectors embedded in nanophotonic circuits," *Nat. Commun.* **3**, 1325 (2012).
- [6] B. Kardynał, Z. Yuan, and A. Shields, "An avalanche-photodiode-based photon-number-resolving detector," *Nat. Photon.* **2**, 425 (2008).
- [7] T. P. Pearsall, *Photonics Essentials* (McGraw-Hill, New York, 2003).
- [8] G. Romero, J. J. García-Ripoll, and E. Solano, "Microwave photon detector in circuit qed," *Phys. Rev. Lett.* **102**, 173602 (2009).
- [9] Y.-F. Chen, D. Hover, S. Sendelbach, L. Maurer, S. T. Merkel, E. J. Pritchett, F. K. Wilhelm, and R. McDermott, "Microwave photon counter based on Josephson junctions," *Phys. Rev. Lett.* **107**, 217401 (2011).
- [10] B. Fan, G. Johansson, J. Combes, G. J. Milburn, and T. M. Stace, "Nonabsorbing high-efficiency counter for itinerant microwave photons," *Phys. Rev. B* **90**, 035132 (2014).

- [11] S. R. Sathyamoorthy, L. Tornberg, A. F. Kockum, B. Q. Baragiola, J. Combes, C. M. Wilson, T. M. Stace, and G. Johansson, “Quantum nondemolition detection of a propagating microwave photon,” *Phys. Rev. Lett.* **112**, 093601 (2014).
- [12] O. Kyriienko and A. S. Sørensen, “Continuous-wave single-photon transistor based on a superconducting circuit,” *Phys. Rev. Lett.* **117**, 140503 (2016).
- [13] X. Gu, A. F. Kockum, A. Miranowicz, Y. xi Liu, and F. Nori, “Microwave photonics with superconducting quantum circuits,” *Phys. Rep.* **718-719**, 1–102 (2017).
- [14] K. Inomata, Z. Lin, K. Koshino, W. D. Oliver, J.-S. Tsai, T. Yamamoto, and Y. Nakamura, “Single microwave-photon detector using an artificial λ -type three-level system,” *Nat. Commun.* **7**, 12303 (2016).
- [15] A. Narla, S. Shankar, M. Hatridge, Z. Leghtas, K. M. Sliwa, E. Zalys-Geller, S. O. Mundhada, W. Pfaff, L. Frunzio, R. J. Schoelkopf, and M. H. Devoret, “Robust concurrent remote entanglement between two superconducting qubits,” *Phys. Rev. X* **6**, 031036 (2016).
- [16] A. Opremcak, I. V. Pechenezhskiy, C. Howington, B. G. Christensen, M. A. Beck, E. Leonard, J. Suttle, C. Wilen, K. N. Nesterov, G. J. Ribeill, T. Thorbeck, F. Schlenker, M. G. Vavilov, B. L. T. Plourde, and R. McDermott, “Measurement of a superconducting qubit with a microwave photon counter,” *Science* **361**, 1239–1242 (2018).
- [17] J.-C. Besse, S. Gasparinetti, M. C. Collodo, T. Walter, P. Kurpiers, M. Pechal, C. Eichler, and A. Wallraff, “Single-shot quantum nondemolition detection of individual itinerant microwave photons,” *Phys. Rev. X* **8**, 021003 (2018).
- [18] S. Kono, K. Koshino, Y. Tabuchi, A. Noguchi, and Y. Nakamura, “Quantum non-demolition detection of an itinerant microwave photon,” *Nat. Phys.* **14**, 546 (2018).
- [19] R. Dassonneville, R. Assouly, T. Peronnin, P. Rouchon, and B. Huard, “Number-resolved photcounter for propagating microwave mode,” *Phys. Rev. Applied* **14**, 044022 (2020).
- [20] A. Essig, Q. Ficheux, T. Peronnin, N. Cottet, R. Lescanne, A. Sarlette, P. Rouchon, Z. Leghtas, and B. Huard, “Multiplexed photon number measurement,” *Phys. Rev. X* **11**, 031045 (2021).
- [21] O. Stanisavljević, J.-C. Philippe, J. Gabelli, M. Aprili, J. Estève, and J. Basset, “Efficient microwave photon-to-electron conversion in a high-impedance quantum circuit,” *Phys. Rev. Lett.* **133**, 076302 (2024).
- [22] L. Balembois, J. Travesedo, L. Pallegoix, A. May, E. Billaud, M. Villiers, D. Estève, D. Vion, P. Bertet, and E. Flurin, “Cyclically operated microwave single-photon counter with sensitivity of 10^{-22} W/ $\sqrt{\text{Hz}}$,” *Phys. Rev. Appl.* **21**, 014043 (2024).
- [23] K. Petrovnin, J. Wang, M. Perelshtein, P. Hakonen, and G. S. Paraoanu, “Microwave photon detection at parametric criticality,” *PRX Quantum* **5**, 020342 (2024).
- [24] S. Haldar, H. Havir, W. Khan, D. Zenelaj, P. P. Potts, S. Lehmann, K. A. Dick, P. Samuelsson, and V. F. Maisi, “High-efficiency microwave photodetection by cavity coupled double dots with single cavity-photon sensitivity,” (2024), arXiv:2406.03047.
- [25] C. H. Wong and M. G. Vavilov, “Quantum efficiency of a single microwave photon detector based on a semiconductor double quantum dot,” *Phys. Rev. A* **95**, 012325 (2017).
- [26] W. Khan, P. P. Potts, S. Lehmann, C. Thelander, K. A. Dick, P. Samuelsson, and V. F. Maisi, “Efficient and continuous microwave photoconversion in hybrid cavity-semiconductor nanowire double quantum dot diodes,” *Nat. Commun.* **12**, 5130 (2021).
- [27] D. Zenelaj, P. P. Potts, and P. Samuelsson, “Full counting statistics of the photocurrent through a double quantum dot embedded in a driven microwave resonator,” *Phys. Rev. B* **106**, 205135 (2022).
- [28] L. Cohen, “Time-frequency distributions-a review,” *Proc. IEEE* **77**, 941 (1989).
- [29] W. Mecklenbrauker and F. Hlawatsch, *The Wigner Distribution : Theory and Applications in Signal Processing* (Elsevier, Amsterdam, 1997).
- [30] L. Childress, A. S. Sørensen, and M. D. Lukin, “Mesoscopic cavity quantum electrodynamics with quantum dots,” *Phys. Rev. A* **69**, 042302 (2004).
- [31] T. Frey, P. J. Leek, M. Beck, A. Blais, T. Ihn, K. Ensslin, and A. Wallraff, “Dipole coupling of a double quantum dot to a microwave resonator,” *Phys. Rev. Lett.* **108**, 046807 (2012).
- [32] C. Bergenfeldt and P. Samuelsson, “Nonlocal transport properties of nanoscale conductor–microwave cavity systems,” *Phys. Rev. B* **87**, 195427 (2013).
- [33] C. Xu and M. G. Vavilov, “Full counting statistics of photons emitted by a double quantum dot,” *Phys. Rev. B* **88**, 195307 (2013).
- [34] N. Lambert, C. Flindt, and F. Nori, “Photon-mediated electron transport in hybrid circuit-qed,” *EPL* **103**, 17005 (2013).
- [35] C. Bergenfeldt, P. Samuelsson, B. Sothmann, C. Flindt, and M. Büttiker, “Hybrid microwave-cavity heat engine,” *Phys. Rev. Lett.* **112**, 076803 (2014).
- [36] Y.-Y. Liu, J. Stehlik, C. Eichler, M. J. Gullans, J. M. Taylor, and J. R. Petta, “Semiconductor double quantum dot micromaser,” *Science* **347**, 285–287 (2015).
- [37] A. Stockklauser, P. Scarlino, J. V. Koski, S. Gasparinetti, C. K. Andersen, C. Reichl, W. Wegscheider, T. Ihn, K. Ensslin, and A. Wallraff, “Strong coupling cavity qed with gate-defined double quantum dots enabled by a high impedance resonator,” *Phys. Rev. X* **7**, 011030 (2017).
- [38] S. Haldar, H. Havir, W. Khan, S. Lehmann, C. Thelander, K. A. Dick, and V. F. Maisi, “Energetics of microwaves probed by double quantum dot absorption,” *Phys. Rev. Lett.* **130**, 087003 (2023).
- [39] S. Haldar, D. Zenelaj, P. P. Potts, H. Havir, S. Lehmann, K. A. Dick, P. Samuelsson, and V. F. Maisi, “Microwave power harvesting using resonator-coupled double quantum dot photodiode,” *Phys. Rev. B* **109**, L081403 (2024).
- [40] A. Faraon, A. Majumdar, and J. Vučković, “Generation of nonclassical states of light via photon blockade in optical nanocavities,” *Phys. Rev. A* **81**, 033838 (2010).
- [41] A. Majumdar, D. Englund, M. Bajcsy, and J. Vučković,

- “Nonlinear temporal dynamics of a strongly coupled quantum-dot–cavity system,” *Phys. Rev. A* **85**, 033802 (2012).
- [42] D. Raserio, A. Portacio, P. Villamil, and B. Rodríguez, “Light transmission from a strongly coupled qd-cavity system driven by a laser pulse,” *Physica E Low Dimens. Syst. Nanostruct.* **129**, 114645 (2021).
- [43] E. T. Jaynes and F. W. Cummings, “Comparison of quantum and semiclassical radiation theories with application to the beam maser,” *Proc. IEEE* **51**, 89 (1963).
- [44] G. Lindblad, “On the generators of quantum dynamical semigroups,” *Commun. Math. Phys.* **48**, 119 (1976).
- [45] H.-P. Breuer and F. Petruccione, *Theory of Open Quantum Systems* (Oxford University Press, USA, 2007).
- [46] S. O. Rice, “Volterra systems with more than one input port—distortion in a frequency converter,” *Bell Syst. Tech. J.* **52**, 1255.
- [47] C. Crespo-Cadenas, M. J. Madero-Ayora, J. Reina-Tosina, and J. Becerra-González, “Formal deduction of a volterra series model for complex-valued systems,” *Signal Processing* **131**, 245 (2017).
- [48] P. P. Hofer, “Quasi-probability distributions for observables in dynamic systems,” *Quantum* **1**, 32 (2017).
- [49] B. Bouachache and F. Rodriguez, “Recognition of time-varying signals in the time-frequency domain by means of the Wigner distribution,” in *ICASSP ’84. IEEE International Conference on Acoustics, Speech, and Signal Processing*, Vol. 9 (1984) pp. 239–242.
- [50] B. Boashash and P. Black, “An efficient real-time implementation of the Wigner-Ville distribution,” *IEEE Trans. Acoust., Speech, Signal. Process.* **35**, 1611 (1987).
- [51] B. Boashash, “Note on the use of the Wigner distribution for time-frequency signal analysis,” *IEEE Trans. Acoust., Speech, Signal. Process.* **36**, 1518 (1988).
- [52] L. Debnath, “The Wigner-Ville distribution and time-frequency signal analysis,” in *Wavelet Transforms and Their Applications* (Birkhäuser Boston, Boston, MA, 2002) pp. 307–360.
- [53] D. Dragoman, “Applications of the Wigner distribution function in signal processing,” *EURASIP J. Adv. Signal Process.* **2005**, 264967 (2005).
- [54] M. Belloni, M. A. Doncheski, and R. W. Robinett, “Wigner quasi-probability distribution for the infinite square well: Energy eigenstates and time-dependent wave packets,” *Am. J. Phys.* **72**, 1183 (2004).
- [55] C. W. Gardiner and M. J. Collett, “Input and output in damped quantum systems: Quantum stochastic differential equations and the master equation,” *Phys. Rev. A* **31**, 3761 (1985).
- [56] D. Ferraro, A. Feller, A. Ghibaudo, E. Thibierge, E. Bocquillon, G. Fève, C. Grenier, and P. Degiovanni, “Wigner function approach to single electron coherence in quantum hall edge channels,” *Phys. Rev. B* **88**, 205303 (2013).
- [57] D. Gabor, “Theory of communication. part 1: The analysis of information,” *Proc. Inst. Electr. Eng.* **93**, 429 (1946).
- [58] H. Toida, T. Nakajima, and S. Komiyama, “Vacuum rabi splitting in a semiconductor circuit qed system,” *Phys. Rev. Lett.* **110**, 066802 (2013).
- [59] A. Bhattacharyya, “On a measure of divergence between two statistical populations defined by their probability distributions,” *Bull. Calcutta Math. Soc.* **35**, 99–109 (1943).
- [60] J. Johansson, P. Nation, and F. Nori, “Qutip: An open-source python framework for the dynamics of open quantum systems,” *Comp. Phys. Comm.* **183**, 1760–1772 (2012).
- [61] D. J. Griffiths and D. F. Schroeter, *Introduction to Quantum Mechanics*, 3rd ed. (Cambridge University Press, 2018).
- [62] R. Merlin, “Rabi oscillations, Floquet states, Fermi’s golden rule, and all that: Insights from an exactly solvable two-level model,” *Am. J. Phys.* **89**, 26–34 (2021).
- [63] K. Fischer, L. Hanschke, M. Kremser, J. Finley, K. Müller, and J. Vuckovic, “Pulsed rabi oscillations in quantum two-level systems: Beyond the area theorem,” *Quantum Science and Technology* **3** (2017), 10.1088/2058-9565/aa9269.
- [64] H. Schlichting and K. Gersten, *Boundary-Layer Theory*, 8th ed. (Springer, 2000).
- [65] A. Stockklauser, V. F. Maisi, J. Basset, K. Cujia, C. Reichl, W. Wegscheider, T. Ihn, A. Wallraff, and K. Ensslin, “Microwave emission from hybridized states in a semiconductor charge qubit,” *Phys. Rev. Lett.* **115**, 046802 (2015).
- [66] Y.-Y. Liu, J. Stehlik, C. Eichler, X. Mi, T. R. Hartke, M. J. Gullans, J. M. Taylor, and J. R. Petta, “Threshold dynamics of a semiconductor single atom maser,” *Phys. Rev. Lett.* **119**, 097702 (2017).
- [67] T. L. van den Berg and P. Samuelsson, “Charge-photon transport statistics and short-time correlations in a single quantum dot–resonator system with an arbitrarily large coupling parameter,” *Phys. Rev. B* **100**, 035408 (2019).
- [68] B. K. Agarwalla, M. Kulkarni, and D. Segal, “Photon statistics of a double quantum dot micromaser: Quantum treatment,” *Phys. Rev. B* **100**, 035412 (2019).
- [69] T. L. Curtright and C. K. Zachos, “Quantum mechanics in phase space,” *Asia Pac. Phys. Newsl.* **01**, 37–46 (2012).